

# A Variational Framework for Phase-Field Fracture Modeling with Applications to Microstructure Fragmentation, Dewatering, Ductile Failure, and Spallation

by

Tianchen Hu

Department of Mechanical Engineering and Materials Science  
Duke University

Date: \_\_\_\_\_  
Approved:

---

John Dolbow, Advisor

---

Wilkins Aquino

---

Johann Guilleminot

---

Manolis Veveakis

---

Benjamin W. Spencer

Dissertation submitted in partial fulfillment of the requirements for the degree of  
Doctor of Philosophy in the Department of Mechanical Engineering and Materials  
Science  
in the Graduate School of Duke University  
2021

## ABSTRACT

A Variational Framework for Phase-Field Fracture Modeling  
with Applications to Microstructure Fragmentation,  
Dessication, Ductile Failure, and Spallation

by

Tianchen Hu

Department of Mechanical Engineering and Materials Science  
Duke University

Date: \_\_\_\_\_  
Approved:

---

John Dolbow, Advisor

---

Wilkins Aquino

---

Johann Guilleminot

---

Manolis Veveakis

---

Benjamin W. Spencer

An abstract of a dissertation submitted in partial fulfillment of the requirements for  
the degree of Doctor of Philosophy in the Department of Mechanical Engineering  
and Materials Science  
in the Graduate School of Duke University  
2021

Copyright © 2021 by Tianchen Hu  
All rights reserved

# Abstract

Lorem ipsum dolor sit amet, consectetur adipiscing elit. Sed porta finibus lacus venenatis varius. Proin luctus, est ac facilisis aliquam, leo est tempus velit, eu euismod mi nunc ut odio. Nulla porttitor velit vel dolor dapibus sollicitudin. Sed lobortis lorem ut dui bibendum pellentesque. Curabitur in volutpat ex, ut semper ipsum. In auctor ac ex euismod aliquet. Ut rutrum neque sed felis auctor luctus. Mauris nec lorem placerat, mattis turpis vel, lacinia purus. Maecenas nunc mauris, semper ut aliquam at, luctus sed justo. Proin porttitor cursus orci. Ut id vehicula massa, ac sagittis lectus. Sed eget justo faucibus, posuere purus.

# Contents

<b>Abstract</b>	<b>iv</b>
<b>List of Tables</b>	<b>vii</b>
<b>List of Figures</b>	<b>viii</b>
<b>Acknowledgements</b>	<b>x</b>
<b>1 Introduction</b>	<b>1</b>
1.1 Background . . . . .	1
1.2 Organization of the dissertation . . . . .	1
1.3 Notation . . . . .	1
<b>2 The Variational Framework</b>	<b>3</b>
2.1 Kinematics and Constraints . . . . .	3
2.2 Thermodynamics . . . . .	5
2.3 The minimization problem . . . . .	10
2.4 Discretization . . . . .	15
<b>3 Brittle and Quasi-Brittle Fracture: Fracture Evolution in Polycrystalline Materials</b>	<b>18</b>
3.1 Introduction . . . . .	18
3.2 Theory . . . . .	20
3.2.1 Constitutive choices . . . . .	20
3.2.2 Approximation of the pressure boundary condition . . . . .	23

3.2.3	Governing equations	25
3.3	Verification	26
3.3.1	Uniaxial traction of a bar	26
3.3.2	Pressurized crack propagation	27
3.4	Numerical examples	29
3.4.1	Predicting the critical fracture strength	29
3.4.2	High burnup structure fragmentation	38
<b>A</b>	<b>Code availability</b>	<b>46</b>
<b>B</b>	<b>On the phase-field irreversibility constraint</b>	<b>47</b>
<b>C</b>	<b>The flooding algorithm for counting fragments</b>	<b>48</b>
	<b>Bibliography</b>	<b>52</b>
	<b>Biography</b>	<b>55</b>

# List of Tables

3.1	Parameters and material properties used in the intergranular fracture simulations . . . . .	31
3.2	Summary of fracture strength obtained from 15 realizations of 3 porosity values. R denotes the realization index. . . . .	38
3.3	Parameters and material properties used in the fission-gas-induced HBS fracture simulations. . . . .	39
C.1	Demonstration of classification after the update from time step n to time step n+1. Broken elements are denoted with an underscore. . . . .	51

# List of Figures

3.1	A bar under uniaxial tension. . . . .	26
3.2	Phase-field variable in initial conditions (for internal length scale $l = 20$ mm). The red and blue color correspond to value of $10^{-3}$ and 0, respectively. . . . .	26
3.3	A bar under uniaxial tension with different pressure values $\bar{p}$ : (a) Reaction force on the left boundary. (b) Reaction force on the right boundary. (c) Regularized pressure value. . . . .	28
3.4	A bar under uniaxial tension with different internal lengths $l$ . . . . .	29
3.5	Sneddon benchmark problem. . . . .	30
3.6	Comparison between the numerical results and the LEFM solution for the critical pressure values. . . . .	31
3.7	(a) The lenticular geometry is described by the length $L$ , the thickness $S$ and the dihedral angle $\phi$ . (b) Gas bubble geometry and boundary conditions. (c) Comparison of stress-strain curves for different gas bubble geometries. . . . .	33
3.8	Final configuration (crack surfaces highlighted in blue) for different loading (a) uniaxial (b) biaxial (c) triaxial. . . . .	34
3.9	Comparison of stress-strain curves for different loading conditions. . .	35
3.10	(a-c) Initial configuration of REVs with an average grain size of $9.4\text{ }\mu\text{m}$ . (d-f) Final configuration (crack surfaces highlighted in blue) for REVs. Different porosity values are considered: (a, d) 2.02%, (b, e) 4.04%, (c, f) 6.06%. . . . .	36
3.11	Comparison of stress-strain curves for different porosity values. . . . .	36

3.12 Variation in normalized fracture strength with changing porosity. In the current chapter, five trial calculations were performed for each porosity level, and each calculation was based on one realization of the spatial distribution of bubbles. The 95% confidence interval is shown in stripes. . . . .	38
3.13 Results for (a-c) the small bubble with radius 0.25 $\mu\text{m}$ and (d-f) the large bubble with radius 0.25 $\mu\text{m}$ (a, d) Pressure history. (b, e) Crack paths superimposed on the voronoi structure. (c, f) Contour plot of the maximum principal stress. . . . .	40
3.14 Results for bubble radius 0.5 $\mu\text{m}$ and external pressure (a-c) 0 MPa, (d-f) 30 MPa, (g-i) 60 MPa. (a, d, g) Pressure history. (b, e, h) Crack paths superimposed on the voronoi structure. (c, f, i) Contour plot of the maximum principal stress. . . . .	41
3.15 Results for (a-b) the two-bubble case and (c-d) the three-bubble case. (a, c) Crack paths superimposed on the voronoi structure. (b, d) Contour plot of the maximum principal stress. . . . .	43
3.16 25 % recrystallization stage: (a) Crack propagation; (b) Maximum principal stress. . . . .	44
3.17 60 % recrystallization stage: (a) Crack propagation; (b) Maximum principal stress. . . . .	44
3.18 100 % recrystallization stage: (a) Crack propagation; (b) Maximum principal stress. . . . .	45
C.1 (a) Final damage field obtained using a spatially correlated random $\mathcal{G}_c$ and $\psi_c$ . (b) Corresponding clusters labeled by the flooding algorithm. Cluster boundaries are marked in black. . . . .	49
C.2 Status change from step n to step n+1. “Broken” elements are labeled in yellow, and “intact” elements are white. The step-by-step reclassification procedure is shown in Table C.1. . . . .	51

# Acknowledgements

I am thankful for the many people.

# 1

## Introduction

Introduction placeholder.

### 1.1 Background

### 1.2 Organization of the dissertation

### 1.3 Notation

In what follows, deterministic scalar, vectors, second-order tensors, and fourth-order tensors are denoted by  $a$  (or  $A$ ),  $\mathbf{a}$  (or  $\mathbf{A}$ ),  $\mathbf{A}$ , and  $\mathbb{A}$ , respectively.

Let  $\Omega$  be a collection of points  $\mathbf{X} \in \mathbb{R}^d$ ,  $d \in \{1, 2, 3\}$ . Scalar- and vector-valued random fields defined on the probability space  $(\Theta, \Sigma, \mathbb{P})$ , indexed by  $\Omega$ , are denoted as  $\{A(\mathbf{X}), \mathbf{X} \in \Omega\}$  and  $\{\mathbf{A}(\mathbf{X}), \mathbf{X} \in \Omega\}$ , respectively. At any fixed material point  $\mathbf{X} \in \Omega$ ,  $a(\mathbf{X})$  and  $\mathbf{a}(\mathbf{X})$  are random variables defined on the probability space  $(\Theta, \Sigma, \mathbb{P})$ . For any fixed  $\theta \in \Theta$ ,  $a(\theta)$  and  $\mathbf{a}(\theta)$  are realizations of the random variables. Similarly,  $\mathbf{X} \mapsto a(\mathbf{X}; \theta)$  and  $\mathbf{X} \mapsto \mathbf{a}(\mathbf{X}; \theta)$  are realizations of the random fields  $\{A(\mathbf{X}), \mathbf{X} \in \Omega\}$  and  $\{\mathbf{A}(\mathbf{X}), \mathbf{X} \in \Omega\}$ .

Einstein summations are assumed wherever applicable unless otherwise stated.

For any vectors  $\mathbf{a}$  and  $\mathbf{b}$  of the same size, the inner product is defined as  $\mathbf{a} \cdot \mathbf{b} = a_i b_i$  where  $a_i$  and  $b_i$  are components of the vectors. The associated vector norm is  $\|\mathbf{a}\|^2 = a \cdot a$ . Similarly, for any second-order tensors  $\mathbf{A}$  and  $\mathbf{B}$  of the same size, the inner product is defined as  $\mathbf{A} : \mathbf{B} = \text{tr}(\mathbf{A}^T \mathbf{B})$ . The associated Frobenius norm writes  $\|\mathbf{A}\|_F = \sqrt{\mathbf{A} : \mathbf{A}}$ .

# 2

## The Variational Framework

### 2.1 Kinematics and Constraints

Let us start by defining degrees of freedom in the system. Let  $\Omega$  be a body consisting of a continuous collection of material points. Let  $\Omega_0 \subset \mathbb{R}^d$  be the reference configuration at some time  $t = t_0$ , whose particles are identified by their position  $\mathbf{X}$ , and  $\Omega_t \subset \mathbb{R}^d$  be the current configuration at a time  $t > t_0$ , with particles at position  $\mathbf{x}$ . Let  $\Phi : \Omega_0 \times [t_0, t] \mapsto \mathbb{R}^d$  be the deformation map. The deformation gradient is denoted as  $\mathbf{F} = \nabla \Phi$ , where the operator  $\nabla$  denotes differentiation with respect to  $\mathbf{X}$  (in the reference configuration  $\Omega_0$ ). The Jacobian determinant of the deformation gradient is written as  $J = \det \mathbf{F}$ .

Throughout this contribution, the *local thermodynamic state* of an infinitesimal material neighborhood is defined by:

- the deformation gradient  $\mathbf{F}$  from the Lie group of invertible and orientation-preserving linear transformations in  $\mathbb{R}^d$ ;
- the collection of internal variables  $\mathbf{Z} \in \mathbb{M}$ , where the set  $\mathbb{M}$  depend on the material;

- the entropy density per unit volume  $s \in \mathbb{R}$  in the reference configuration;

Plastic (or creep) deformations are modeled through the framework of multiplicative decomposition

$$\mathbf{F} = \mathbf{F}^e \mathbf{F}^p \mathbf{F}^g, \quad (2.1)$$

where  $\mathbf{F}^e$ ,  $\mathbf{F}^p$  are referred to as the elastic and plastic deformation gradients, respectively.  $\mathbf{F}^g$  is the product of eigen deformation gradients. For example, isotropic thermal expansion can be accounted for by  $\mathbf{F}^g = (1 + \alpha \Delta T) \mathbf{I}$ , where  $\alpha$  is the thermal expansion coefficient, and  $\Delta T = T - T_0$  is the temperature change from the reference temperature  $T_0$ .

Crack surfaces are regularized and modeled using a phase-field  $d$ ,  $0 \leq d \leq 1$ , where  $d = 0$  represents the intact state of a material point, and  $d = 1$  indicates the material point has lost all of its load-carrying capacity.

For the systems of interest in this contribution, the internal variables are considered to be the plastic deformation  $\mathbf{F}^p$  (from the same Lie group of  $\mathbf{F}$ ), the (scalar) effective plastic strain  $\bar{\varepsilon}^p \in \mathbb{R}_+$ , and the phase-field  $d$  regularizing the crack surfaces, i.e.

$$\mathbf{Z} = \{\mathbf{F}^p, \bar{\varepsilon}^p, d\}. \quad (2.2)$$

In general, internal variables evolve subject to constraints of the following form

$$\mathbf{L}(\mathbf{Z}) \dot{\mathbf{Z}} = \mathbf{0}. \quad (2.3)$$

The specific form of the constraint depends on physical requirements and the material class. For isotropic  $J_2$ -plasticity, the Prandtl-Reuss flow rule requires

$$\text{tr} \left( \dot{\mathbf{F}}^p \mathbf{F}^{p-1} \right) = 0, \quad (2.4a)$$

$$\left\| \dot{\mathbf{F}}^p \mathbf{F}^{p-1} \right\|^2 - \frac{3}{2} |\dot{\varepsilon}^p|^2 = 0, \quad (2.4b)$$

where (2.4a) requires the plastic flow to be isochoric, and (2.4b) normalizes the effective plastic strain  $\bar{\varepsilon}^p$  to be uniaxial. Furthermore, the plastic flow is assumed to be irreversible in the sense

$$\dot{\bar{\varepsilon}}^p \geq 0. \quad (2.5)$$

Since the phase-field variable  $d$  is an approximation to the irreversible crack set, and as will be shown later, the crack geometric function is a monotonically increasing function of  $d$ , it is intuitive to impose the irreversibility constraint on the phase-field variable, i.e.

$$\dot{d} \geq 0. \quad (2.6)$$

Note that (2.4a), (2.4b), (2.5), and (2.6) are all of the general form (2.3).

## 2.2 Thermodynamics

Recall that the motions of the body are described by the deformation mapping  $\Phi : \Omega_0 \times [t_0, t] \mapsto \mathbb{R}^d$ . Let  $\rho_0$  be the density in the reference configuration,  $\mathbf{b}$  be the distributed body force per unit mass,  $\mathbf{P}$  be the first Piola-Kirchhoff stress,  $\mathbf{n}_0$  be the outward normal in the reference configuration,  $u$  be the internal energy density,  $k = \rho_0 \dot{\Phi} \cdot \dot{\Phi}$  be the kinetic energy density,  $\mathcal{P}^{\text{ext}}$  be the external power expenditure,  $s$  be the entropy density,  $q$  be the distributed heat source per unit mass, and  $\mathbf{h}$  be the heat flux. The densities  $u$ ,  $k$  and  $s$  are all defined per unit volume in the reference configuration. The motions of the body must obey the following conservations and thermodynamic laws:

- Conservation of mass:

$$\frac{d}{dt} \int_{\Omega'} \rho_0 \, dV = 0. \quad (2.7)$$

- Conservation of linear momentum:

$$\frac{d}{dt} \int_{\Omega'} \rho_0 \dot{\Phi} dV = \int_{\Omega'} \rho_0 \mathbf{b} dV + \int_{\partial\Omega'} \mathbf{P} \mathbf{n}_0 dA. \quad (2.8)$$

- Conservation of angular momentum:

$$\frac{d}{dt} \int_{\Omega'} \Phi \times (\rho_0 \dot{\Phi}) dV = \int_{\Omega'} \Phi \times (\rho_0 \mathbf{b}) dV + \int_{\partial\Omega'} \Phi \times (\mathbf{P} \mathbf{n}_0) dA. \quad (2.9)$$

- The first law of thermodynamics:

$$\frac{d}{dt} \int_{\Omega'} u dV + \frac{d}{dt} \int_{\Omega'} k dV = \int_{\Omega'} \mathcal{P}^{\text{ext}} dV + \int_{\Omega'} \rho_0 q dV - \int_{\partial\Omega'} \mathbf{h} \cdot \mathbf{n}_0 dA. \quad (2.10)$$

- The second law of thermodynamics:

$$\frac{d}{dt} \int_{\Omega'} s dV - \int_{\Omega'} \frac{\rho_0 q}{T} dV + \int_{\partial\Omega'} \frac{\mathbf{h} \cdot \mathbf{n}_0}{T} dA \geq 0. \quad (2.11)$$

All the above conservation and thermodynamic laws hold for any arbitrary subbody  $\Omega' \subset \Omega$ , hence they can be written in the following local form:

$$\dot{\rho}_0 = 0, \quad (2.12a)$$

$$\rho_0 \mathbf{a} = \nabla \cdot \mathbf{P} + \rho_0 \mathbf{b}, \quad (2.12b)$$

$$\mathbf{P} \mathbf{F} = \mathbf{F} \mathbf{P}^T, \quad (2.12c)$$

$$\dot{u} + \dot{k} = \mathcal{P}^{\text{ext}} + \rho_0 q - \nabla \cdot \mathbf{h}, \quad (2.12d)$$

$$\dot{s}^{\text{int}} = \dot{s} - \frac{\rho_0 q}{T} + \nabla \cdot \frac{\mathbf{h}}{T} \geq 0. \quad (2.12e)$$

Alternatively, local form of the second law can be written in terms of the internal energy density as

$$\dot{s}^{\text{int}} = \mathcal{P}^{\text{ext}} - \dot{u} - \frac{1}{T} \mathbf{h} \cdot \nabla T. \quad (2.13)$$

For convenience, the collection of thermodynamic state variables (working with the Helmholtz free energy), kinematic degrees of freedom, and internal variables are defined as

$$\mathcal{S} = \{\mathcal{K}, T\}, \quad \mathcal{K} = \{\boldsymbol{\Phi}, \mathbf{Z}\}, \quad \mathbf{Z} = \{\mathbf{F}^p, \bar{\varepsilon}^p, d\}. \quad (2.14)$$

The rates of change of the kinematic variables are denoted as  $\mathcal{V} = \{\dot{\boldsymbol{\Phi}}, \dot{\mathbf{F}}^p, \dot{\bar{\varepsilon}}^p, \dot{d}\}$ .

The generalized velocities of the kinematic state variables are collected in the set

$$\dot{\Lambda} = \{\dot{\boldsymbol{\Phi}}, \dot{\mathbf{F}}, \dot{\mathbf{F}}^p, \dot{\bar{\varepsilon}}^p, \dot{d}, \nabla \dot{d}\}. \quad (2.15)$$

Recall that the local thermodynamic state is assumed to be depend only on  $\boldsymbol{\Phi}$ ,  $\mathbf{Z}$  and  $s$ , i.e.

$$u = \hat{u}(\Lambda, s), \quad T = \hat{T}(\Lambda, s). \quad (2.16)$$

It is convenient to work with the Helmholtz free energy density (per unit volume) with  $T$  as a state variable by introducing the Legendre transformation

$$\psi(\Lambda, T) = \inf_s [u(\Lambda, s) - Ts]. \quad (2.17)$$

The local form of the second law can then be rewritten using the identity  $\dot{\psi} = \dot{u} - \dot{T}s$  and the fact that  $\mathcal{P}^{\text{ext}} = \mathcal{P}^{\text{int}}$ :

$$\dot{s}^{\text{int}} = \delta - \frac{1}{T} \mathbf{h} \cdot \nabla T, \quad \delta = \mathcal{P}^{\text{int}} - \dot{\psi} - \dot{T}s. \quad (2.18)$$

where  $\delta$  shall be referred to as the internal dissipation density (per unit volume).

Combining (2.12e) and (2.18) yields the energy balance in the *entropy form*:

$$T\dot{s} = \rho_0 q - \nabla \cdot \mathbf{h} + \delta. \quad (2.19)$$

The internal power expenditure  $\mathcal{P}^{\text{int}}$  can be expressed in terms of generalized forces as

$$\mathcal{P}^{\text{int}} = \mathbf{P} : \dot{\mathbf{F}} + \mathbf{T} : \dot{\mathbf{F}}^p + Y \dot{\bar{\varepsilon}}^p + f \dot{d} + \boldsymbol{\xi} \cdot \nabla \dot{d}. \quad (2.20)$$

It is assumed that each of the generalized forces can be additively decomposed into an equilibrium part, thermodynamically conjugate to the Helmholtz free energy density, and a viscous part, i.e.

$$\mathbf{P} = \mathbf{P}^{\text{eq}}(\Lambda, T) + \mathbf{P}^{\text{vis}}(\dot{\mathbf{F}}, T; \Lambda), \quad (2.21\text{a})$$

$$\mathbf{T} = \mathbf{T}^{\text{eq}}(\Lambda, T) + \mathbf{T}^{\text{vis}}(\dot{\mathbf{F}}^p, T; \Lambda), \quad (2.21\text{b})$$

$$Y = Y^{\text{eq}}(\Lambda, T) + Y^{\text{vis}}(\dot{\varepsilon}^p, T; \Lambda), \quad (2.21\text{c})$$

$$f = f^{\text{eq}}(\Lambda, T) + f^{\text{vis}}(\dot{d}, T; \Lambda), \quad (2.21\text{d})$$

$$\boldsymbol{\xi} = \boldsymbol{\xi}^{\text{eq}}(\Lambda, T) + \boldsymbol{\xi}^{\text{vis}}(\nabla \dot{d}, T; \Lambda), \quad (2.21\text{e})$$

where the viscous forces vanish as the rate diminishes to preclude viscous dissipation in quasi-static processes, i.e.

$$\lim_{\|\dot{\mathbf{F}}\| \rightarrow 0^+} \mathbf{P}^{\text{vis}} = 0, \quad (2.22\text{a})$$

$$\lim_{\|\dot{\mathbf{F}}^p\| \rightarrow 0^+} \mathbf{T}^{\text{vis}} = 0, \quad (2.22\text{b})$$

$$\lim_{|\dot{\varepsilon}^p| \rightarrow 0^+} Y^{\text{vis}} = 0, \quad (2.22\text{c})$$

$$\lim_{|\dot{d}| \rightarrow 0^+} f^{\text{vis}} = 0, \quad (2.22\text{d})$$

$$\lim_{\|\nabla \dot{d}\| \rightarrow 0^+} \boldsymbol{\xi}^{\text{vis}} = 0. \quad (2.22\text{e})$$

For convenience, the equilibrium forces and the viscous forces are collected in the sets

$$\mathcal{F}^{\text{eq}} = \{\mathbf{P}^{\text{eq}}, \mathbf{T}^{\text{eq}}, Y^{\text{eq}}, f^{\text{eq}}, \boldsymbol{\xi}^{\text{eq}}\}, \quad \mathcal{F}^{\text{vis}} = \{\mathbf{P}^{\text{vis}}, \mathbf{T}^{\text{vis}}, Y^{\text{vis}}, f^{\text{vis}}, \boldsymbol{\xi}^{\text{vis}}\}. \quad (2.23)$$

The rate of the Helmholtz free energy density can be expanded as

$$\dot{\psi} = \psi_{,\mathbf{F}} : \dot{\mathbf{F}} + \psi_{,\mathbf{F}^p} : \dot{\mathbf{F}}^p + \psi_{,\dot{\varepsilon}^p} \dot{\varepsilon}^p + \psi_{,d} \dot{d} + \psi_{,\nabla d} \cdot \nabla \dot{d} + \psi_{,T} \dot{T}. \quad (2.24)$$

Inserting the identity (2.24) into (2.18) and applying the Coleman-Noll procedure

lead to several thermodynamic restrictions on the constitutive relations:

$$\begin{aligned} \mathbf{P}^{\text{eq}} &= \psi_{,\mathbf{F}}, & \mathbf{T}^{\text{eq}} &= \psi_{,\mathbf{F}^p}, & Y^{\text{eq}} &= \psi_{,\bar{\varepsilon}^p}, & f^{\text{eq}} &= \psi_{,d}, & \boldsymbol{\xi}^{\text{eq}} &= \psi_{,\nabla d}, & -s &= \psi_{,T}. \end{aligned} \quad (2.25)$$

Substituting (2.25) and (2.24) into (2.18) simplifies the definition of the internal dissipation density:

$$\delta = \mathbf{P}^{\text{vis}} : \dot{\mathbf{F}} + \mathbf{T}^{\text{vis}} : \dot{\mathbf{F}}^p + Y^{\text{vis}} \dot{\bar{\varepsilon}}^p + f^{\text{vis}} \dot{d} + \boldsymbol{\xi}^{\text{vis}} \cdot \nabla d. \quad (2.26)$$

Using the identities (2.24) and (2.25), the rate of the entropy density can be expanded as

$$\dot{s} = -\dot{\psi}_{,T} = -\mathbf{P}_{,T}^{\text{eq}} : \dot{\mathbf{F}} - \mathbf{T}_{,T}^{\text{eq}} : \dot{\mathbf{F}}^p - Y_{,T}^{\text{eq}} \dot{\bar{\varepsilon}}^p - f_{,T}^{\text{eq}} \dot{d} - \boldsymbol{\xi}_{,T}^{\text{eq}} \cdot \nabla d - \psi_{,TT} \dot{T}. \quad (2.27)$$

By introducing the heat capacity per unit mass at constant  $\Lambda$ :

$$\rho_0 c_v = -T \psi_{,TT}, \quad (2.28)$$

the energy balance (2.19) can be rewritten as

$$\rho_0 c_v \dot{T} = \rho_0 q - \nabla \cdot \mathbf{h} + \delta + \delta_T, \quad (2.29)$$

where  $\delta_T$  is the dissipation density accounting for the thermal effects in the thermodynamic conjugates:

$$\delta_T = T \left( \mathbf{P}_{,T}^{\text{eq}} : \dot{\mathbf{F}} + \mathbf{T}_{,T}^{\text{eq}} : \dot{\mathbf{F}}^p + Y_{,T}^{\text{eq}} \dot{\bar{\varepsilon}}^p + f_{,T}^{\text{eq}} \dot{d} + \boldsymbol{\xi}_{,T}^{\text{eq}} \cdot \nabla d \right), \quad (2.30)$$

e.g.  $T \mathbf{P}_{,T}^{\text{eq}} : \dot{\mathbf{F}}$  is the dissipation accounting for thermoelastic effects, and  $T Y_{,T}^{\text{eq}} \dot{\bar{\varepsilon}}^p$  is the dissipation accounting for thermoplastic softening.

## 2.3 The minimization problem

In this section, we construct a potential such that *all* the conservation and thermodynamic laws can be derived (if not implied by construction) from a minimization problem. First, we assume that the Helmholtz free energy density  $\psi$  can be additively decomposed into a strain-energy density  $\psi^e$ , a plastic energy density  $\psi^p$ , a fracture energy density  $\psi^f$ , and a thermal energy density  $\psi^h$ :

$$\psi = \psi^e(\mathbf{F}, \mathbf{F}^p, d, T) + \psi^p(\bar{\varepsilon}^p, d, T) + \psi^f(d, \nabla d, T) + \psi^h(T). \quad (2.31)$$

To maintain a variational structure, the viscous forces are supposed to be derived from dual kinetic potentials.

**Example** (The elastic dual kinetic potential). Suppose there exist a potential  $\zeta(\mathbf{P}^{\text{vis}})$  such that

$$\dot{\mathbf{F}} = \zeta_{,\mathbf{P}^{\text{vis}}}. \quad (2.32)$$

The dual kinetic potential is introduced by applying the Legendre transformation:

$$\psi^{e*}(\dot{\mathbf{F}}) = \sup_{\mathbf{P}^{\text{vis}}} \left[ \mathbf{P}^{\text{vis}} : \dot{\mathbf{F}} - \zeta \right], \quad (2.33)$$

where it follows immediately that

$$\mathbf{P}^{\text{vis}} = \psi^{e*}_{,\dot{\mathbf{F}}}. \quad (2.34)$$

Note that the symbol  $\psi^{e*}$  is chosen in line with the energetic counterpart of the potential, not to imply that  $\psi^{e*}$  is the Legendre transformation of  $\psi^e$ . In fact,  $\psi^{e*}$  is the Legendre transformation of  $\zeta$ .

Following the foregoing example, the viscous forces are defined as

$$\mathbf{P}^{\text{vis}} = \psi^{e*}_{,\dot{\mathbf{F}}}, \quad \mathbf{T}^{\text{vis}} = \psi^{p*}_{,\dot{\mathbf{F}}^p}, \quad \mathbf{Y}^{\text{vis}} = \psi^{p*}_{,\dot{\varepsilon}^p}, \quad \mathbf{f}^{\text{vis}} = \psi^{f*}_{,d}, \quad \boldsymbol{\xi}^{\text{vis}} = \psi^{f*}_{,\nabla d}, \quad (2.35)$$

where  $\psi^{e*}$  is the elastic dual kinetic potential describing rate-sensitivity of the deformation, e.g. Newtonian viscosity;  $\psi^{p*}$  is the plastic dual kinetic potential describing

the rate-sensitivity of cold work, e.g. viscoplasticity;  $\psi^{f*}$  is the fracture dual kinetic potential describing viscous regularization of fracture propagation.

To satisfy the second law (2.13), the material is assumed to be *strictly dissipative* in the sense that every thermodynamic process results in an increase in entropy for nonzero rates, i.e.  $\mathcal{F}^{\text{dis}} \cdot \dot{\Lambda} > \mathbf{0}$ ,  $\forall \dot{\Lambda} \neq 0$ . These constraints are subject to later verification.

The external power expenditure  $\mathcal{P}^{\text{ext}}(\dot{\Phi}, T)$  is defined as

$$\begin{aligned} \mathcal{P}^{\text{ext}} = & \underbrace{\int_{\Omega_0} \rho_0 \mathbf{b} \cdot \dot{\Phi} \, dV}_{\text{body force}} + \underbrace{\int_{\partial_t \Omega_0} \mathbf{t} \cdot \dot{\Phi} \, dA}_{\text{surface traction}} + \underbrace{\int_{\partial_h \Omega_0} \bar{h}_n \ln \left( \frac{T}{T_0} \right) \, dA}_{\text{external heat flux}} \\ & + \underbrace{\int_{\partial_r \Omega_0} h \left[ T - T_0 \ln \left( \frac{T}{T_0} \right) \right] \, dA}_{\text{external heat convection}} - \underbrace{\int_{\Omega_0} \rho_0 q \ln \left( \frac{T}{T_0} \right) \, dV}_{\text{heat source}}, \end{aligned} \quad (2.36)$$

where the subscripts in  $\partial_t$ ,  $\partial_h$  and  $\partial_r$  denote the corresponding subsets of the surface with the associated Neumann/Robin boundary conditions.  $\bar{h}_n$  is the heat flux,  $h$  is the heat transfer coefficient, and  $T_0$  is the reference or the ambient temperature.

To account for heat generation due to dissipations (i.e. from dual kinetic potentials), it is necessary to introduce the concept of the *equilibrium temperature* corresponding to the thermodynamic state  $\{\Lambda, s\}$  defined as

$$T^{\text{eq}} = u_{,s}(\Lambda, s), \quad (2.37)$$

and the *external temperature*  $T$ , along with a dummy integration factor  $T/T^{\text{eq}}$ . It will be shown later that the equilibrium temperature will be equal to the external temperature at equilibrium, and that the integration factor brings the effect of dissipation mechanisms into heat generation.

The total potential is constructed such that given the current kinematic state variables  $\Lambda$  and the current temperature, the velocities  $\mathcal{V}$  and the rate of temperature

change can be obtained as a critical point following the first variations, which can then be used to update the state variables. The total potential  $L$  is constructed as

$$L(\dot{\Lambda}, \dot{s}, T, \nabla T) = \int_{\Omega_0} \varphi(\dot{\Lambda}, \dot{s}, T) \, dV - \mathcal{P}^{\text{ext}}(\dot{\Lambda}, T), \quad (2.38a)$$

$$\varphi(\dot{\Lambda}, \dot{s}, T, \nabla T) = \dot{u}(\dot{\Lambda}) + \dot{u}(\dot{\Lambda}, \dot{s}) + \Delta^* \left( \frac{T}{T^{\text{eq}}} \dot{\Lambda}, T^{\text{eq}} \right) - T \dot{s} - \chi(\mathbf{g}), \quad (2.38b)$$

where  $\dot{u}$  is the rate of change in the internal energy,  $\dot{s}$  is the rate of change in the entropy,  $\Delta^*$  is the sum of dual kinetic potentials:

$$\Delta^*(\dot{\Lambda}, T; \Lambda) = \psi^{e*}(\dot{\mathbf{F}}, T; \Lambda) + \psi^{p*}(\dot{\mathbf{F}}^p, \dot{\varepsilon}^p, T; \Lambda) + \psi^{f*}(\dot{d}, \nabla \dot{d}, T; \Lambda), \quad (2.39)$$

and  $\chi$  is the Fourier potential defined in terms of the normalized temperature gradient  $\mathbf{g} = -\frac{1}{T} \nabla T$ , with the property  $-\mathbf{h} = \chi_{,\mathbf{g}}$ . Finally, the entire problem can be cast variational into the following inf-sup problem as

$$(\mathcal{V}, \dot{s}, T) = \arg \left[ \inf_{\mathcal{V}, \dot{s}} \sup_T L(\dot{\Lambda}, \dot{s}, T, \nabla T) \right]. \quad (2.40)$$

Owing to [1, 2], the solutions of (2.40) have the following properties: Assume  $\Omega_0$  is open and bounded with only Dirichlet boundary conditions, and let  $\hat{T} \equiv \ln(T/T_0)$ ,  $\hat{T} \in \mathbb{R}$ . If  $\chi$  is convex in  $\nabla \hat{T}$  and grows as a power  $|\nabla \hat{T}|^p$ ,  $1 < p < \infty$ , then  $L(\dot{\Lambda}, \dot{s}, T)$  attains its supremum  $L(\dot{\Lambda}, \dot{s})$  in the Sobolev space  $W^{1,p}(\Omega_0)$ . If  $\chi$  is *strictly convex* in  $\nabla u$ , then the solution  $T$  is unique. The existence of the solution  $\dot{\Lambda}$  is endorsed by the polyconvexity of the potentials  $\dot{u}(\dot{\Lambda}, \dot{s})$  and  $\Delta^*(\dot{\Lambda})$ . In addition, the dissipation inequality (e.g. (2.12e)) is satisfied if  $\Delta^*(\dot{\Lambda}, T)$  attains its infimum for every  $\dot{\Lambda}$  when the rate is zero.

**Remark.** One may attempt to state the variational inf-sup problem without relying on the concept of the equilibrium temperature, the external temperature, and the integration factor:

$$(\mathcal{V}, \dot{s}, T) = \arg \left[ \inf_{\mathcal{V}, \dot{s}} \sup_T L'(\dot{\Lambda}, \dot{s}, T, \nabla T) \right], \quad (2.41a)$$

$$L'(\dot{\Lambda}, \dot{s}, T, \nabla T) = \int_{\Omega_0} \varphi'(\dot{\Lambda}, \dot{s}, T, \nabla T) \, dV - \mathcal{P}^{\text{ext}}(\dot{\Lambda}, T), \quad (2.41b)$$

$$\varphi'(\dot{\Lambda}, \dot{s}, T, \nabla T) = k(\dot{\Phi}) + \dot{u}(\dot{\Lambda}, \dot{s}) + \Delta^*(\dot{\Lambda}, T) - T\dot{s} - \chi(\mathbf{g}). \quad (2.41c)$$

However, it immediately follows that the supremum of (2.41a) in  $T$  does not include contributions from dissipation mechanisms:

$$\rho_0 c_v \dot{T} = \rho_0 q - \nabla \cdot \mathbf{h}, \quad (2.42)$$

which clearly violates the first law of thermodynamics (2.29).

To find the critical points of the inf-sup problem (2.40), we first isolate the local state variables from the global state variables. That is, (2.40) can be reorganized as

$$(\mathcal{V}, \dot{s}, T) = \arg \left[ \inf_{\dot{\Phi}, \dot{d}} \sup_T L \left( \inf_{\dot{\mathbf{F}}^p, \dot{\varepsilon}^p, \dot{s}} \varphi \right) \right], \quad (2.43)$$

since the updates of  $\mathbf{F}^p$ ,  $\dot{\varepsilon}^p$  and  $s$  can be performed point-wise. Expanding  $\dot{u}$  in (2.38b) and substituting the constitutive restrictions (2.25) yield

$$\begin{aligned} \varphi(\dot{\Lambda}, \dot{s}, T, \nabla T) &= \rho_0 \mathbf{a} \cdot \dot{\Phi} + \mathbf{P}^{\text{eq}} : \dot{\mathbf{F}} + \mathbf{T}^{\text{eq}} : \dot{\mathbf{F}}^p + Y^{\text{eq}} \dot{\varepsilon}^p + f^{\text{eq}} \dot{d} + \boldsymbol{\xi}^{\text{eq}} \cdot \nabla \dot{d} \\ &\quad + T^{\text{eq}} \dot{s} + \Delta^* \left( \frac{T}{T^{\text{eq}}} \dot{\Lambda}, T^{\text{eq}} \right) - T \dot{s} - \chi(\mathbf{g}). \end{aligned} \quad (2.44)$$

The minimizer in  $\dot{s}$  follows as

$$T^{\text{eq}} - T = 0. \quad (2.45)$$

The infimum in  $\dot{\mathbf{F}}^p$  and  $\dot{\varepsilon}^p$  shall follow from the joint minimization problem subject

to the flow rule (2.3), i.e.

$$\begin{aligned} \left( \dot{\mathbf{F}}^p, \dot{\bar{\varepsilon}}^p \right) = \arg \inf_{\dot{\mathbf{F}}^p, \dot{\bar{\varepsilon}}^p} & \left[ \mathbf{T}^{\text{eq}} : \dot{\mathbf{F}}^p + Y^{\text{eq}} \dot{\bar{\varepsilon}}^p + \Delta^* \right] \\ \text{subject to} & \quad \mathbf{L}(\mathbf{Z}) \dot{\mathbf{Z}} = \mathbf{0}. \end{aligned} \quad (2.46)$$

To find the infimum in  $T$ , substitute the definition of the free energy (2.31), the definition of the dual kinetic potential (2.39), the definition of the external power (2.36), and the constitutive restrictions (2.25) into (2.38a) to obtain

$$\begin{aligned} L(\dot{\Lambda}, \dot{s}, T, \nabla T) = & \int_{\Omega_0} \left[ \rho_0 \mathbf{a} \cdot \dot{\boldsymbol{\phi}} + \mathbf{P}^{\text{eq}} : \dot{\mathbf{F}} + \mathbf{T}^{\text{eq}} : \dot{\mathbf{F}}^p + Y^{\text{eq}} \dot{\bar{\varepsilon}}^p + f^{\text{eq}} \dot{d} \right. \\ & \left. + \boldsymbol{\xi}^{\text{eq}} \cdot \nabla \dot{d} + T^{\text{eq}} \dot{\Lambda}, T^{\text{eq}} \right] - T \dot{s} - \chi(\mathbf{g}) \, dV \\ & - \int_{\Omega_0} \rho_0 \mathbf{b} \cdot \dot{\boldsymbol{\phi}} \, dV - \int_{\partial_t \Omega_0} \mathbf{t} \cdot \dot{\boldsymbol{\phi}} \, dA - \int_{\partial_h \Omega_0} \bar{h}_n \ln \left( \frac{T}{T_0} \right) \, dA \\ & - \int_{\partial_r \Omega_0} h \left[ T - T_0 \ln \left( \frac{T}{T_0} \right) \right] \, dA + \int_{\Omega_0} \rho_0 q \ln \left( \frac{T}{T_0} \right) \, dV \end{aligned} \quad (2.47)$$

The variation of (2.47) in  $T$  in the admissible space (admissible with respect to Dirichlet boundary conditions) is

$$T \dot{s} = \rho_0 q - \nabla \cdot \mathbf{h} + \delta, \quad \forall \mathbf{X} \in \Omega_0, \quad (2.48a)$$

$$\mathbf{h} \cdot \mathbf{n}_0 = \bar{h}_n, \quad \forall \mathbf{X} \in \partial_h \Omega_0, \quad (2.48b)$$

$$\mathbf{h} \cdot \mathbf{n}_0 = h(T - T_0), \quad \forall \mathbf{X} \in \partial_r \Omega_0. \quad (2.48c)$$

With the substitution of (2.27) and the definition of heat capacity (2.28), the first law in the form of (2.29) is recovered

$$\rho_0 c_v \dot{T} = \rho_0 q - \nabla \cdot \mathbf{h} + \delta + \delta_T. \quad (2.49)$$

Next, the balance of linear momentum and traction boundary conditions are recov-

ered from variations in the admissible fields of  $\dot{\Phi}$ :

$$\rho_0 \mathbf{a} = \nabla \cdot \mathbf{P} + \mathbf{b}, \quad \forall \mathbf{X} \in \Omega_0, \quad (2.50a)$$

$$\mathbf{P} \mathbf{n}_0 = \mathbf{t}, \quad \forall \mathbf{X} \in \partial_t \Omega_0. \quad (2.50b)$$

Finally, variation in the admissible space of  $\dot{d}$  yields the fracture evolution equation on the inactive set

$$\nabla \cdot \boldsymbol{\xi} - f = 0, \quad \forall \mathbf{X} \in \mathcal{I}(\Omega_0), \quad (2.51)$$

$$\boldsymbol{\xi} \cdot \mathbf{n}_0 = 0, \quad \forall \mathbf{X} \in \mathcal{I}(\partial_d \Omega_0). \quad (2.52)$$

## 2.4 Discretization

We begin this section by summarizing the strong form of the general initial boundary value problem of interest:

**The initial boundary value problem for the time interval  $t \in I = [t_0, t_f]$**

Linear momentum balance: $\rho_0 \mathbf{a} = \nabla \cdot \mathbf{P} + \rho_0 \mathbf{b},$	$\Omega_0 \times ]t_0, t[,$
$\mathbf{P} \mathbf{n}_0 = \mathbf{t},$	$\partial_t \Omega_0 \times ]t_0, t[,$
$\boldsymbol{\Phi} = \boldsymbol{\Phi}_g,$	$\partial_u \Omega_0 \times ]t_0, t[,$
Fracture evolution: $\nabla \cdot \boldsymbol{\xi} - f = 0,$	$\mathcal{I}_t(\Omega_0) \times ]t_0, t[,$
$\boldsymbol{\xi} \cdot \mathbf{n}_0 = 0,$	$\mathcal{I}_t(\partial_d \Omega_0) \times ]t_0, t[,$
Heat transfer: $\rho_0 c_v \dot{T} = \rho_0 q - \nabla \cdot \mathbf{h} + \delta + \delta_T,$	$\Omega_0 \times ]t_0, t[,$
$\mathbf{h} \cdot \mathbf{n}_0 = \bar{h}_n,$	$\partial_h \Omega_0 \times ]t_0, t[,$
$\mathbf{h} \cdot \mathbf{n}_0 = h(T - T_0),$	$\partial_r \Omega_0 \times ]t_0, t[,$
$T = T_g,$	$\partial_T \Omega_0 \times ]t_0, t[,$
Initial conditions: $\boldsymbol{\Phi} = \boldsymbol{\Phi}_0,$	$\Omega_0, t = t_0,$
$\dot{\boldsymbol{\Phi}} = \mathbf{v}_0,$	$\Omega_0, t = t_0,$
$d = d_0,$	$\Omega_0, t = t_0,$
$T = T_0,$	$\Omega_0, t = t_0.$

The yield surface and the flow rule (and their corresponding constitutive updates)

are defined only after specific constitutive assumptions are made in the following chapters (e.g. ??).

To derive the weak form, we begin by introducing the trial spaces  $\mathcal{U}_t$ ,  $\mathcal{D}_t$  and  $\mathcal{T}_t$

$$\mathcal{U}_t = \{\boldsymbol{\Phi} \in \mathcal{H}^1(\Omega_0)^d \mid \mathbf{u} = \mathbf{u}_g \text{ on } \partial_u \Omega_0\}, \quad (2.53a)$$

$$\mathcal{D}_t = \{d \in \mathcal{H}^1(\Omega_0) \mid \dot{d} > 0 \text{ on } \mathcal{I}_t(\Omega_0)\}, \quad (2.53b)$$

$$\mathcal{T}_t = \{T \in \mathcal{H}^1(\Omega_0) \mid T = T_g \text{ on } \partial_T \Omega_0\}, \quad (2.53c)$$

and the weighting spaces  $\mathcal{V}$ ,  $\mathcal{C}$  and  $\mathcal{E}$

$$\mathcal{V} = \{\mathbf{w} \in \mathcal{H}^1(\Omega_0)^d \mid \mathbf{w} = \mathbf{0} \text{ on } \partial_u \Omega_0\}, \quad (2.54a)$$

$$\mathcal{C} = \{c \in \mathcal{H}^1(\Omega_0)\}, \quad (2.54b)$$

$$\mathcal{E} = \{e \in \mathcal{H}^1(\Omega_0) \mid T = 0 \text{ on } \partial_T \Omega_0\}. \quad (2.54c)$$

The weak form can be derived as:

### The weak form

Given parameters in the IBVP, find  $\boldsymbol{\Phi} \in \mathcal{U}_t$ ,  $d \in \mathcal{D}_t$  and  $T \in \mathcal{T}_t$ ,  $t \in [t_0, t_f]$ , such that  $\forall \mathbf{w} \in \mathcal{V}$ ,  $\forall c \in \mathcal{C}$  and  $\forall e \in \mathcal{E}$ ,

$$(\mathbf{w}, \rho_0 \mathbf{a}) + (\nabla \mathbf{w}, \mathbf{P}) - (\mathbf{w}, \rho_0 \mathbf{b}) - \langle \mathbf{w}, \mathbf{t} \rangle_{\partial_t \Omega_0} = 0, \quad (2.55a)$$

$$(\nabla c, \boldsymbol{\xi}) + (c, f) = 0, \quad (2.55b)$$

$$\begin{aligned} - \left( e, \rho_0 c_v \dot{T} \right) + (e, \rho_0 q) + (\nabla e, \mathbf{h}) + (e, \delta + \delta_T) \\ - \langle e, \bar{h}_n \rangle_{\partial_h \Omega_0} - \langle e, h(T - T_0) \rangle_{\partial_r \Omega_0} = 0, \end{aligned} \quad (2.55c)$$

with projections of initial conditions

$$(\mathbf{w}, \boldsymbol{\Phi} - \boldsymbol{\Phi}_0) = 0, \quad (2.56a)$$

$$\left( \mathbf{w}, \dot{\boldsymbol{\Phi}} - \mathbf{v}_0 \right) = 0, \quad (2.56b)$$

$$(c, d - d_0) = 0, \quad (2.56c)$$

$$(e, T - T_0) = 0. \quad (2.56d)$$

Using the Galerkin method, with finite dimensional function spaces  $\tilde{\mathcal{U}}_t \subset \mathcal{U}_t$ ,  $\tilde{\mathcal{V}} \subset \mathcal{V}$ ,  $\tilde{\mathcal{D}}_t \subset \mathcal{D}_t$ ,  $\tilde{\mathcal{C}} \subset \mathcal{C}$ ,  $\tilde{\mathcal{T}}_t \subset \mathcal{T}_t$ ,  $\tilde{\mathcal{E}} \subset \mathcal{E}$ , we arrive at the spatially discrete form of the problem:

## The semidiscrete Galerkin form

Given parameters in the IBVP, find  $\Phi^h \in \tilde{\mathcal{U}}_t$ ,  $d^h \in \tilde{\mathcal{D}}_t$  and  $T^h \in \tilde{\mathcal{T}}_t$ ,  $t \in [t_0, t_f]$ , such that  $\forall \mathbf{w}^h \in \tilde{\mathcal{V}}$ ,  $\forall q^h \in \tilde{\mathcal{C}}$  and  $\forall e^h \in \tilde{\mathcal{E}}$ ,

$$(\mathbf{w}^h, \rho_0 \mathbf{a}) + (\nabla \mathbf{w}^h, \mathbf{P}) - (\mathbf{w}^h, \rho_0 \mathbf{b}) - \langle \mathbf{w}^h, \mathbf{t} \rangle_{\partial_t \Omega_0} = 0, \quad (2.57a)$$

$$(\nabla c^h, \boldsymbol{\xi}) + (c^h, f) = 0, \quad (2.57b)$$

$$\begin{aligned} & - (e^h, \rho_0 c_v \dot{T}) + (e^h, \rho_0 q) + (\nabla e^h, \mathbf{h}) + (e^h, \delta + \delta_T) \\ & - \langle e^h, \bar{h}_n \rangle_{\partial_h \Omega_0} - \langle e^h, h(T^h - T_0) \rangle_{\partial_r \Omega_0} = 0, \end{aligned} \quad (2.57c)$$

with projections of initial conditions

$$(\mathbf{w}^h, \Phi^h - \Phi_0) = 0, \quad (2.58a)$$

$$(\mathbf{w}^h, \dot{\Phi} - \mathbf{v}_0) = 0, \quad (2.58b)$$

$$(c^h, d^h - d_0) = 0, \quad (2.58c)$$

$$(e^h, T^h - T_0) = 0. \quad (2.58d)$$

The discrete inequality for crack irreversibility is satisfied node-wise with a primal-dual active set strategy. See e.g. Heister et al. [3] for implementational details of such a solver. The solver is also generally available in numerical toolboxes, e.g. PETSc [4]. The discrete approximation is calculated using a fixed-point iterative solution scheme outlined from [5]. The semidiscrete momentum balance equation (2.57a) is further discretized using the generalized- $\alpha$  method. The semidiscrete fracture evolution equation (2.57b) and the heat conduction equation (2.57c) are further discretized using the backward-Euler time integration. Discretizations of the plasticity constitutive updates are discussed in ??.

# 3

## Brittle and Quasi-Brittle Fracture: Fracture Evolution in Polycrystalline Materials

### 3.1 Introduction

During the operation of commercial light water reactors, fission of uranium dioxide ( $\text{UO}_2$ ) produces a variety of fission products within the fuel matrix. The fracture behavior of brittle materials is strongly influenced by their underlying microstructural features such as gas bubbles, second-phase particles, pre-existing micro-cracks, grains, grain boundaries, etc. For example, the bubbles at the grain boundaries alter the fracture properties, and subsequently affects the pellet-cladding mechanical interaction (PCMI), fission gas release and swelling. Therefore, it is important to develop a fracture model that incorporates the effects of microstructural features to better understand how fission changes the fracture response of the nuclear fuel.

On the other hand, to improve the economics of commercial nuclear power production, utilities are seeking to increase the allowable burnup limit for  $\text{UO}_2$  fuel. A main factor contributing to the current burnup limit in commercial light-water reactors is the risk of fragmentation during a loss-of-coolant accident (LOCA). To allow

the industry to pursue an increased burnup limit and develop mitigation strategies, an improved capability for predicting the onset of fragmentation is essential.

A thorough review of high-burnup fuel fragmentation is provided in [6]. In the current work, we focus on the fine fragmentation that results in fuel fragments typically less than 0.1 mm in size. It has been reported that fine fragmentation primarily occurs at high burnups—especially when the high-burnup structure (HBS) has formed. The HBS is typically characterized by small newly formed grains with sizes of 100–300 nm and round fission gas pores of micrometric size [7]. It is hypothesized that over-pressurization of fission gas bubbles in the UO<sub>2</sub> HBS could result in fine fragmentation during typical LOCA transients.

In general, fuel fracture can be modeled using phenomenological [8] and mechanical models [9]. Various criteria have been used to determine whether fine fragmentation will occur during a LOCA, but such criteria are all based on simple analytical models [10, 11]. For additional insights into gas-bubble-induced fracture in polycrystalline materials and HBS fine fragmentation (including crack topology, fragment morphology, and fragment topography), a physics-based model is needed to simulate over-pressurization of fission gas bubbles.

Recently, the phase-field fracture models have been applied to study gas-bubble-induced fracture in polycrystalline materials. Chakraborty et al. [12] developed a hierarchical multi-scale approach to model microstructure-sensitive brittle fracture, and 2D simulations are performed to relate fracture strength to porosity. Often-times a 2D approximation over-simplifies the actual microstructure and results in inaccurate measurement of porosity. Diehl et al. [13] proposed 3D models of damage evolution around a single bubble and investigated the influence of the bubble geometry on the fracture response. 3D simulations provide important insights into the influence of porosity on fracture. In this chapter, a phase-field fracture model is employed to address intergranular cracking with multiple bubbles on the grain

boundaries in 3D and is used to model over-pressurized fission-gas-induced fragmentation at the microstructural level.

In HBS, following crack initiation, the cracks will fill with fission gas, and the crack surfaces will become pressurized. To account for pressurized crack surfaces, we present an extension of the quasi-brittle model by including regularized external work done by pressure into the total energy of the system. The regularized external work can be derived either based on a phase-field approximation of the sharp interface [14], or by modifying the free energy in a Biot system via an indicator function based on the phase-field [15]. In this chapter, the former approach is used to derive the phase-field model for brittle and quasi-brittle fracture with pressurized cracks.

## 3.2 Theory

### 3.2.1 Constitutive choices

Following the variational framework presented in Chapter 2, to account for elastic deformation and fracture in polycrystalline materials, the Helmholtz free energy density is decomposed as

$$\psi = \psi^e + \psi^f. \quad (3.1)$$

Recall that  $\psi^e$  is the strain energy density, and  $\psi^f$  is the fracture energy density.

#### *Strain energy density*

For small deformation elasticity considered in this chapter, the state variable  $\Phi$  enters the strain energy density only through the infinitesimal strain tensor

$$\boldsymbol{\varepsilon} = \frac{1}{2} (\nabla \Phi + \nabla^T \Phi). \quad (3.2)$$

The material is assumed to be isotropic, characterized by the Lamé parameter  $\lambda$  and the shear modulus  $G$ . The strain energy density is defined as

$$\psi^e = g\psi_{\langle A \rangle}^e + \psi_{\langle I \rangle}^e, \quad (3.3a)$$

$$\psi_{\langle A \rangle}^e = \frac{1}{2}\lambda \langle \text{tr}(\boldsymbol{\varepsilon}) \rangle_+^2 + G\boldsymbol{\varepsilon}^+ : \boldsymbol{\varepsilon}^+, \quad (3.3b)$$

$$\psi_{\langle I \rangle}^e = \frac{1}{2}\lambda \langle \text{tr}(\boldsymbol{\varepsilon}) \rangle_-^2 + G\boldsymbol{\varepsilon}^- : \boldsymbol{\varepsilon}^-, \quad (3.3c)$$

where  $g = \hat{g}(d)$  is the degradation function to be defined in Section 3.2.1, and  $\boldsymbol{\varepsilon}^\pm$  denotes the positive or the negative part of the strain projected onto the spectrum associated with positive or negative eigenvalues. In the context of small deformation, the Cauchy stress  $\boldsymbol{\sigma}$  can be viewed as the thermodynamic conjugate to the infinitesimal strain  $\boldsymbol{\varepsilon}$ , and can be written as

$$\boldsymbol{\sigma} = \psi_{,\boldsymbol{\varepsilon}}^e = g\boldsymbol{\sigma}_{\langle A \rangle} + \boldsymbol{\sigma}_{\langle I \rangle}, \quad (3.4a)$$

$$\boldsymbol{\sigma}_{\langle A \rangle} = \lambda \langle \text{tr}(\boldsymbol{\varepsilon}) \rangle_+ \mathbf{I} + 2G\boldsymbol{\varepsilon}^+, \quad (3.4b)$$

$$\boldsymbol{\sigma}_{\langle I \rangle} = \lambda \langle \text{tr}(\boldsymbol{\varepsilon}) \rangle_- \mathbf{I} + 2G\boldsymbol{\varepsilon}^-. \quad (3.4c)$$

### *Fracture energy density*

With a sharp crack set  $\Gamma$ , the fracture energy is defined as  $\Psi^f = \int_{\Gamma} \mathcal{G}_c \, dA$ , where  $\mathcal{G}_c$  is the fracture toughness. An approximation of the sharp crack set using a phase-field can be written as

$$\Psi^f \approx \int_{\Omega_0} \mathcal{G}_c \gamma_l(d, \nabla d) \, dV, \quad (3.5)$$

where  $\gamma_l$  is often referred to as the crack surface density parameterized by a regularization length  $l$ . An Allen-Cahn type approximation can be expressed as

$$\gamma_l(d, \nabla d) = \frac{1}{c_0 l} (\alpha + l^2 \nabla d \cdot \nabla d), \quad (3.6)$$

where  $\alpha = \hat{\alpha}(d)$  is the crack geometric function. According to the discussion in Chapter 2, existence requires  $\hat{\alpha}(d)$  to be convex in  $d$ , and the phase-field irreversibility condition (2.6) assumes  $\hat{\alpha}(d)$  attains its minimum at  $d = 0$ .

In the current variational framework, the fracture response, e.g. the critical fracture strength and the softening behavior, is determined by the crack geometric function and the degradation function. In this chapter, to model brittle fracture, where crack only nucleates at stress singularities, i.e.  $\psi_c \rightarrow \infty$ , the following combination of crack geometric function and degradation function is used,

$$\alpha = d^2, \quad g = (1 - d)^2. \quad (3.7)$$

To model quasi-brittle fracture in polycrystalline materials, where the post-fracture behavior can be characterized by certain softening law, the following combination is used,

$$\alpha = \xi d - (1 - \xi)d^2, \quad g = \frac{1}{1 + \phi}, \quad \phi = \frac{a_1 d + a_1 a_2 d^2 + a_1 a_2 a_3 d^3}{(1 - c)^p}, \quad (3.8)$$

where  $\psi_c$  is the critical fracture energy density,  $\alpha$  is parameterized by  $\xi$  ( $\xi$  is conveniently its derivative at  $d = 0$ ), and the degradation function  $g$  is parameterized by  $p$ ,  $a_1$ ,  $a_2$  and  $a_3$ . Based on 1-D analyses, the optimal profile of the phase-field is controlled by  $\xi$ . For a given  $\xi$ , the approximated traction-separation law is determined by  $p$ ,  $a_1$ ,  $a_2$  and  $a_3$ . In this chapter, the following parameters are chosen:

$$\xi = 2, \quad p = 2, \quad a_1 = \frac{\mathcal{G}_c}{c_0 l \psi_c}, \quad a_2 = -\frac{1}{2}, \quad a_3 = 0, \quad (3.9)$$

such that the phase-field is compactly supported by a constant half interfacial width of  $D_u = \frac{\pi}{2}l$ , and a linear traction-separation law is approximated with a slope of  $-\frac{E\psi_c}{\mathcal{G}_c}$ .

### 3.2.2 Approximation of the pressure boundary condition

Starting from the sharp representation of the crack set, the external power expenditure on the crack set due to pressure can be written as

$$\mathcal{P}^{\text{ext}} = \int_{\Gamma} \bar{p} \mathbf{n}_0 \cdot \dot{\Phi} \, dA, \quad (3.10)$$

where  $\bar{p}$  is the magnitude of the pressure. Following [14], the external work is approximated as per:

$$\begin{aligned} \mathcal{P}^{\text{ext}} &= \int_{\Omega_0} \rho^{\text{ext}} \, dV = \int_{\Omega_0} \bar{p} \left( -\frac{\nabla d}{\|\nabla d\|} \right) \cdot \dot{\Phi} \|\nabla I\| \, dV \\ &= \int_{\Omega_0} \bar{p} \left( -\frac{\nabla d}{\|\nabla d\|} \right) \cdot \dot{\Phi} \|\nabla d\| I_{,d} \, dV = - \int_{\Omega_0} \bar{p} \nabla d \cdot \dot{\Phi} I_{,d} \, dV \end{aligned} \quad (3.11)$$

where the surface normal  $\mathbf{n}$  is approximated using the gradient of the phase-field, and a crack indicator function  $I(d) \in C^1([0, 1])$  is introduced so that the approximation respects the  $\Gamma$ -convergence properties.

**Remark.** Based on (3.11), the effective pressure approximated by the phase-field can be defined as:

$$\tilde{p} = \int_{\Omega_0} \frac{\partial \rho^{\text{ext}}}{\partial \dot{\Phi}} \cdot \left( -\frac{\nabla d}{\|\nabla d\|} \right) \, dV = \int_{\Omega_0} \bar{p} \|\nabla I\| \, dV \quad (3.12)$$

Assuming that  $I(0) = 0$  and  $I(1) = 1$ , the proof of  $\Gamma$ -convergence can be sketched via the following method. Consider the approximated external power expenditure due to pressure (parameterized by the phase-field regularization length  $l$ ). The phase-field profile can always be expressed by  $d = \bar{d}(d_{\Gamma}(\mathbf{X})/l)$ , where  $d_{\Gamma}(\mathbf{X})$  is the unsigned distance function for the crack set  $\Gamma$  [16]. Substituting the phase-field profile into

(3.11) yields:

$$\begin{aligned}\mathcal{P}^{\text{ext}} &= - \int_{\Omega_0} \bar{p} \nabla \tilde{d} \cdot \dot{\Phi} I_d(\tilde{d}) \, dV = - \int_{\Omega_0} \bar{p} \nabla I \cdot \dot{\Phi} \, dV \\ &= - \int_{\Omega_0} \bar{p} \frac{dI}{d(d_\Gamma/l)} \frac{1}{l} \nabla d_\Gamma(\mathbf{X}) \cdot \dot{\Phi} \, dV.\end{aligned}\quad (3.13)$$

The domain integral can be converted to a set of path integrals along the level set (phase-field), using the co-area formula, as follows:

$$\mathcal{P}^{\text{ext}} = - \int_0^\infty \int_{\{\mathbf{X} \in \Omega_0, d_\Gamma(\mathbf{X}) = r\}} \bar{p} \frac{dI}{d(r/l)} \frac{1}{l} \nabla d_\Gamma(\mathbf{X}) \cdot \dot{\Phi} \, ds \, dr \quad (3.14)$$

A simple change of variables with  $\tilde{r} = r/l$  yields:

$$\begin{aligned}\mathcal{P}^{\text{ext}} &= - \int_0^\infty \left( \int_{\{\mathbf{X} \in \Omega_0, d_\Gamma(\mathbf{X}) = r\}} \bar{p} \nabla d_\Gamma(\mathbf{X}) \cdot \dot{\Phi} \, ds \right) \frac{dI}{d(r/l)} \frac{1}{l} \, dr \\ &= - \int_0^\infty \left( \int_{\{\mathbf{X} \in \Omega_0, d_\Gamma(\mathbf{X}) = l\tilde{r}\}} \bar{p} \nabla d_\Gamma(\mathbf{X}) \cdot \dot{\Phi} \, ds \right) \frac{dI}{d\tilde{r}} \, d\tilde{r}\end{aligned}\quad (3.15)$$

Next, as the phase-field regularization length diminishes (i.e.,  $l \rightarrow 0$ ), the approximation of the pressure power expenditure converges to:

$$\lim_{l \rightarrow 0} \mathcal{P}^{\text{ext}} = - \int_0^\infty \frac{dI}{d\tilde{r}} \, d\tilde{r} \left[ \int_{\Gamma^+} \bar{p}(-\mathbf{n}_0) \cdot \dot{\Phi} \, dA + \int_{\Gamma^-} \bar{p}(-\mathbf{n}_0) \cdot \dot{\Phi} \, dA \right] \quad (3.16a)$$

where it is apparent that the path integral along the level set converges to the surface integral on two opposite sides of the crack surface, while the gradient of the unsigned distance function converges to the normal on the crack surfaces  $\Gamma$  (i.e.,  $\lim_{l \rightarrow 0} \nabla d_\Gamma(\mathbf{X}) = -\mathbf{n}_0(\mathbf{X})$ ). Recall that the support of the phase-field depends on

the form of the crack geometric function  $\alpha$  [16]; the integral shall be split according to the the ultimate phase-field half interfacial width  $D_u$ :

$$\begin{aligned}
& \lim_{l \rightarrow 0} \mathcal{P}^{\text{ext}} \\
&= - \left( \int_0^{D_u/l} \frac{dI}{d\tilde{r}} d\tilde{r} + \int_{D_u/l}^{\infty} \frac{dI}{d\tilde{r}} d\tilde{r} \right) \left[ \int_{\Gamma^+} \bar{p}(-\mathbf{n}_0) \cdot \dot{\Phi} dA + \int_{\Gamma^-} \bar{p}(-\mathbf{n}_0) \cdot \dot{\Phi} dA \right] \\
&= - \left[ I\left(\tilde{r} = \frac{D_u}{l}\right) - I(\tilde{r} = 0) \right] \left[ \int_{\Gamma^+} \bar{p}(-\mathbf{n}_0) \cdot \dot{\Phi} dA + \int_{\Gamma^-} \bar{p}(-\mathbf{n}_0) \cdot \dot{\Phi} dA \right] \quad (3.17) \\
&= - [I(0) - I(1)] \left[ \int_{\Gamma^+} \bar{p}(-\mathbf{n}_0) \cdot \dot{\Phi} dA + \int_{\Gamma^-} \bar{p}(-\mathbf{n}_0) \cdot \dot{\Phi} dA \right]
\end{aligned}$$

Finally, recall our previous restrictions on the indicator function  $I(c)$ ; the limit reduces to:

$$\lim_{l \rightarrow 0} \mathcal{P}^{\text{ext}} = \int_{\Gamma^+} \bar{p}(-\mathbf{n}_0) \cdot \dot{\Phi} dA + \int_{\Gamma^-} \bar{p}(-\mathbf{n}_0) \cdot \dot{\Phi} dA. \quad (3.18)$$

### 3.2.3 Governing equations

Following the variational framework, substituting (3.1), (3.3a), (3.5), (3.6), and (3.11) into the problem statement (2.40), under the isothermal conditions, the governing equations can be obtained as

$$\nabla \cdot \boldsymbol{\sigma} - \bar{p} \nabla dI_{,d} = \mathbf{0}, \quad (3.19)$$

$$\nabla \cdot \boldsymbol{\xi} - f = 0, \quad (3.20)$$

supplemented by the constitutive relations (3.4a) and

$$\boldsymbol{\xi} = \frac{2\mathcal{G}_c l}{c_0}, \quad f = g_{,d} \psi_{\langle A \rangle}^e + \frac{\mathcal{G}_c}{c_0 l} \alpha_{,d}. \quad (3.21)$$

### 3.3 Verification

#### 3.3.1 Uniaxial traction of a bar

We first verify the uniaxial response of the quasi-brittle fracture model with pressurization. Consider a bar of length  $L = 400$  mm and width  $W = 2$  mm that is subject to uniaxial tension. Plane strain conditions are assumed to hold. A similar example without crack pressurization can be found in [16]. Boundary conditions are shown in Figure 3.1. Both ends of the bar are subject to monotonically increasing horizontal displacements. Only a quarter of the domain is simulated utilizing the two symmetry conditions. The domain is uniformly discretized using QUAD4 elements, with 200 elements along the length and 1 element along the width. Included are the Young's modulus  $E = 3 \times 10^4$  MPa, Poisson's ratio  $\nu = 0.2$ , critical fracture strength  $\psi_c = 1.5 \times 10^{-4}$  mJ mm $^{-3}$ , fracture toughness  $\mathcal{G}_c = 0.12$  mJ mm $^{-2}$ , and the Griffith's characteristic length  $l_{ch} = \frac{\mathcal{G}_c}{2\psi_c} = 400$  mm.

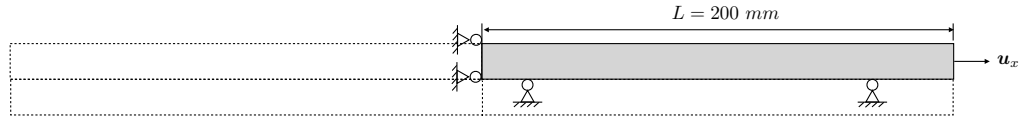


FIGURE 3.1. A bar under uniaxial tension.

---

FIGURE 3.2. Phase-field variable in initial conditions (for internal length scale  $l = 20$  mm). The red and blue color correspond to value of  $10^{-3}$  and 0, respectively.

An arbitrarily small imperfection,  $d_0 = \mathcal{O}(\epsilon)$ , is introduced on the left side of the computational domain to induce localization (Figure 3.2). To study the effect of the pressure, different pressure values

$$\bar{p} \in \{0.2 \text{ MPa}, 0.4 \text{ MPa}, 0.6 \text{ MPa}, 0.8 \text{ MPa}, 1 \text{ MPa}\}$$

are considered, with a fixed phase-field regularization length of  $l = 20$  mm. In the context of fuel fracture, the pressure on the crack surfaces can result from a pressurized gas environment. The reaction force on the left boundary in Figure 3.3a shows that softening occurs simultaneously for different pressure values. With a larger pressure value, the damage grows more quickly. As is seen in Figure 3.3b, the reaction force on the right boundary is balanced with the prescribed pressure once the crack has fully developed. Figure 3.3c plots the approximated effective pressure  $\tilde{p}$  (3.12), which shows good agreement with prescribed values  $\bar{p}$ .

Wu [16] demonstrated that the numerical results are independent of the phase-field regularization length for a quasi-brittle fracture model without pressure [16]. Here, we consider a series of values of phase-field regularization length

$$l \in \{5 \text{ mm}, 10 \text{ mm}, 20 \text{ mm}, 50 \text{ mm}\}$$

with a fixed pressure of  $\bar{p} = 0.4$  MPa. Figure 3.4 reveals the softening behaviors to be essentially the same, regardless of the chosen regularization length  $l$ . This feature allows for choosing  $\mathcal{G}_c$  and  $\psi_c$  values independently from the regularization length.

### 3.3.2 Pressurized crack propagation

Next, we verify fracture propagation conditions predicted by the quasi-brittle fracture model using a benchmark problem proposed by Wilson and Landis [17]. This problem serves to verify whether cracks should propagate once a critical pressure loading is applied. In Figure 3.5d, an initial crack is prescribed in the center with a length of  $2a$ . As shown in Figure 3.5a, the phase-field is initialized to be 1.0 only for those nodes on the bottom boundary belonging to the crack set, the phase-field variable is regularized to satisfy the governing equations, as shown in Figure 3.5b. Note that this differs from the approach suggested in [17, 18] which involves imposing initial values for a set of elements. Utilizing the symmetry, only half of the domain with

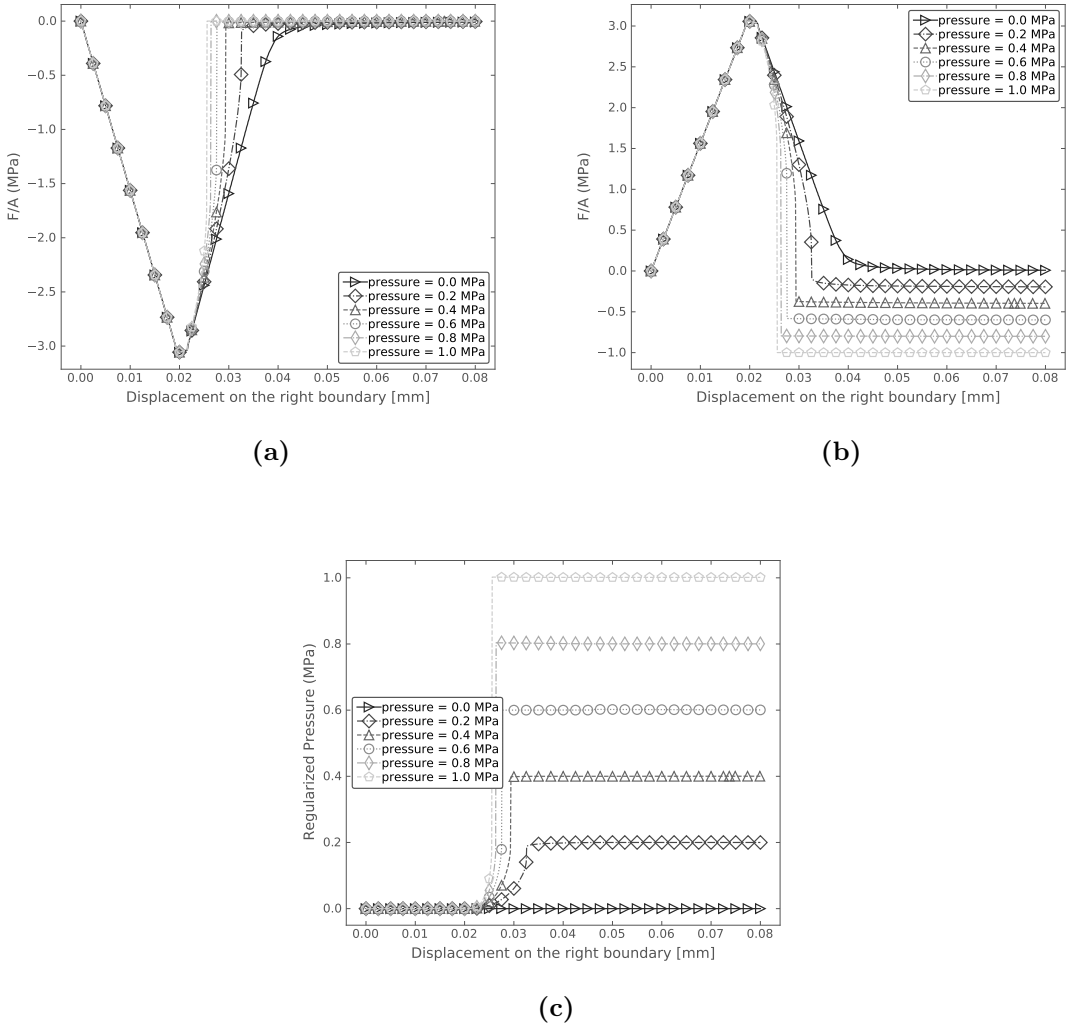


FIGURE 3.3. A bar under uniaxial tension with different pressure values  $\bar{p}$ : (a) Reaction force on the left boundary. (b) Reaction force on the right boundary. (c) Regularized pressure value.

size  $L \times L/2$  is used (Figure 3.5c). The ratio  $L/a$  is taken to be 20. All outer surfaces are fixed. A prescribed pressure is increased until the crack starts to propagate. The propagation of the crack at fixed pressure conditions is unstable. According to the linear elastic fracture mechanics (LEFM) solution, the normalized critical pressure

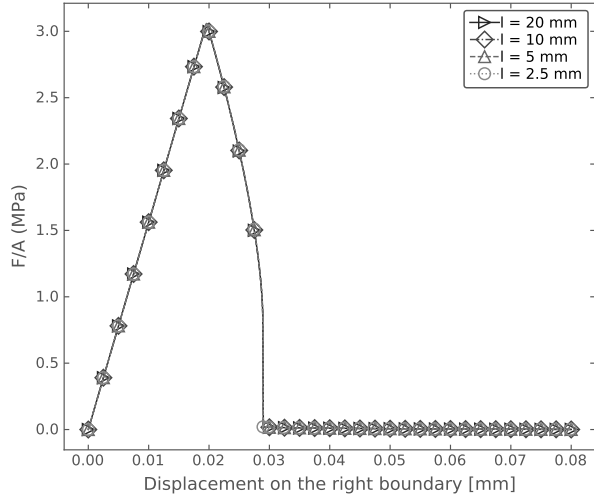


FIGURE 3.4. A bar under uniaxial tension with different internal lengths  $l$ .

is given as:

$$\frac{p_c}{\sigma_0} = \sqrt{\frac{l}{\pi a}}, \quad \sigma_0 = \sqrt{\frac{E}{(1 - \nu^2)} \frac{\mathcal{G}_c^{\text{eff}}}{l}}, \quad (3.22)$$

where  $\mathcal{G}_c^{\text{eff}}$  is the effective fracture toughness in the phase-field fracture model and is given as [19, 18]:

$$\mathcal{G}_c^{\text{eff}} = \mathcal{G}_c \left( \frac{h}{4c_0 l} + 1 \right). \quad (3.23)$$

Note that the LEFM solution is based on a brittle fracture model. A comparison between the numerical results and the LEFM solution for the critical pressure values is shown in Figure 3.6. The phase-field solution converges as  $\psi_c$  increases, and shows good agreement with the LEFM solution.

## 3.4 Numerical examples

### 3.4.1 Predicting the critical fracture strength

This phase-field for brittle fracture model is readily applicable to three dimensional intergranular fracture. In this section, as an example, we simulate UO<sub>2</sub> intergranular

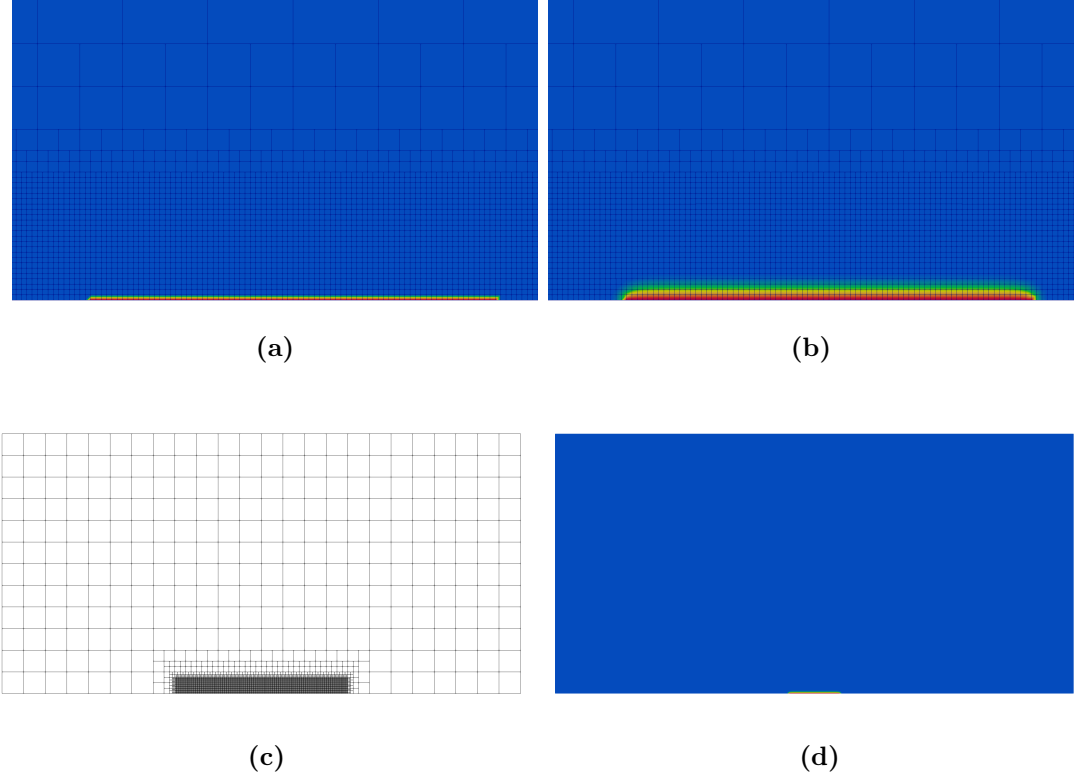


FIGURE 3.5. Pressurized crack propagation problem: (a) Initial values are imposed on crack surface nodes (zoomed view). (b) Regularized phase-field variable after one time step (zoomed view). (c) Mesh with five levels of local refinement. (d) Pre-existing crack. The red and blue color correspond to value of 1.0 and 0, respectively.

fracture and compare with experimental results. Material properties and model parameters are summarized in Table 3.3. We show how the presence of gas bubbles can alter the critical fracture strength of the specimen. The fracture toughness  $\mathcal{G}_c^b = 2 \times 10^{-3} \text{ mJ mm}^{-2}$  is calibrated based on Molecular Dynamics simulations [12], and is assumed to be homogeneous over the grain boundaries.

Without further calibration, to facilitate intergranular crack propagation, the fracture toughness of grain need to satisfy  $\mathcal{G}_c^g \gg \mathcal{G}_c^b$  so that crack propagation is predominately driven by intergranular elastic energy. In this chapter, the polycrystalline microstructure is described by a set of non-conserved variables in a diffuse manner, obtained from a phase field grain growth model [21]. The phase-field  $\phi_i = 1$

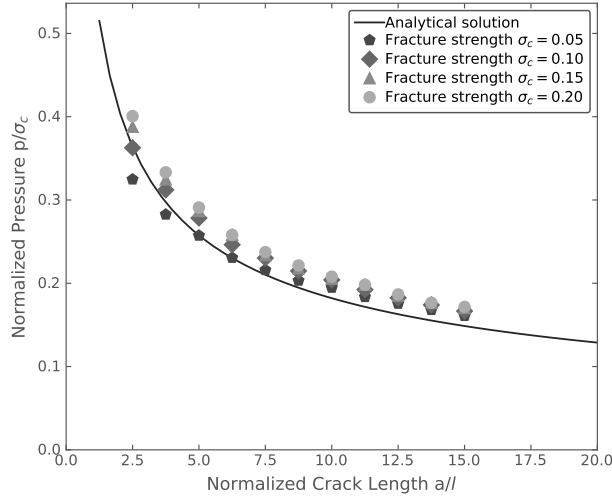


FIGURE 3.6. Comparison between the numerical results and the LEFM solution for the critical pressure values.

**Table 3.1.** Parameters and material properties used in the intergranular fracture simulations

Property	Symbol	Value	Unit	Reference
Young's modulus	$E$	385	GPa	[20]
Grain boundary fracture toughness	$\mathcal{G}_c^b$	0.002	$\text{mJ mm}^{-2}$	[12]
Grain fracture toughness	$\mathcal{G}_c^g$	0.01	$\text{mJ mm}^{-2}$	
Phase-field regularization length	$l$	0.5	$\mu\text{m}$	

within the  $i$ -th grain, and  $\phi_i = 0$  elsewhere. Regions where  $\phi_i$  varies between 0 and 1 correspond to grain boundaries. The grain boundaries are computed as  $B = \sum \phi_i^2$ .

The fracture toughness  $\mathcal{G}_c$  is then defined as

$$\mathcal{G}_c(\mathbf{X}) = \begin{cases} \mathcal{G}_c^b, & B(\mathbf{X}) < \bar{B}, \\ \mathcal{G}_c^g, & B(\mathbf{X}) \geq \bar{B}, \end{cases} \quad (3.24)$$

where  $\bar{B}$  is the threshold to distinguish between grains and grain boundaries. For simulations considered in this chapter,  $\bar{B} = 0.75$  has been observed to be an appropriate choice. In this chapter, the elastic properties for the grain is assumed to be isotropic, e.g. independent of the crystal orientations. An arbitrarily small Young's

modulus of  $10^{-9}E$  is assigned to the bubbles to remove zero energy modes. The domain is uniformly discretized with HEX8 elements with element size of  $0.25\text{ }\mu\text{m}$ .

### *Effect of gas bubble geometry*

Gas bubbles on the grain boundaries act as crack initiators, and an accurate representation of their geometry is necessary to capture the stress concentration on the interface between the bubbles and the grain boundaries.

In equilibrium, gas bubbles on the grain boundaries have a lenticular shape. A 2D schematic of the lenticular bubble is shown in Figure 3.7a. The lenticular geometry is characterized by its length, thickness and dihedral angle. The dihedral angle is determined by the ratio of grain boundary energy to surface energy and it can vary over a wide range for  $\text{UO}_2$  [22, 23].

To study the effect of gas bubble geometry on the critical fracture strength, three frequently adopted geometries are considered:

- (i) A lenticular gas bubble with length  $22.4\text{ }\mu\text{m}$ , thickness  $16\text{ }\mu\text{m}$  and dihedral angle  $142.6^\circ$ .
- (ii) A lenticular gas bubble with length  $22.4\text{ }\mu\text{m}$ , thickness  $10\text{ }\mu\text{m}$  and dihedral angle  $96.6^\circ$ .
- (iii) A spherical gas bubble with radius  $7.9\text{ }\mu\text{m}$  which has the same volume as the lenticular gas bubble.

Consider a representative elementary volume (REV) with side length  $120\text{ }\mu\text{m}$ . The gas bubbles are placed over the grain boundaries such that the middle plane of the lenticular- or spherical- shaped bubbles are tangent to the grain boundaries. Symmetric boundary conditions are prescribed and a uniform displacement is applied on the top of the REV.

The variations in the critical fracture strength (Figure 3.7c) suggest that the shape of gas bubble affects the predicted fracture properties. A lenticular-shaped bubble has higher stress concentration at the edges of grain boundary bubbles, which lowers the critical fracture strength.

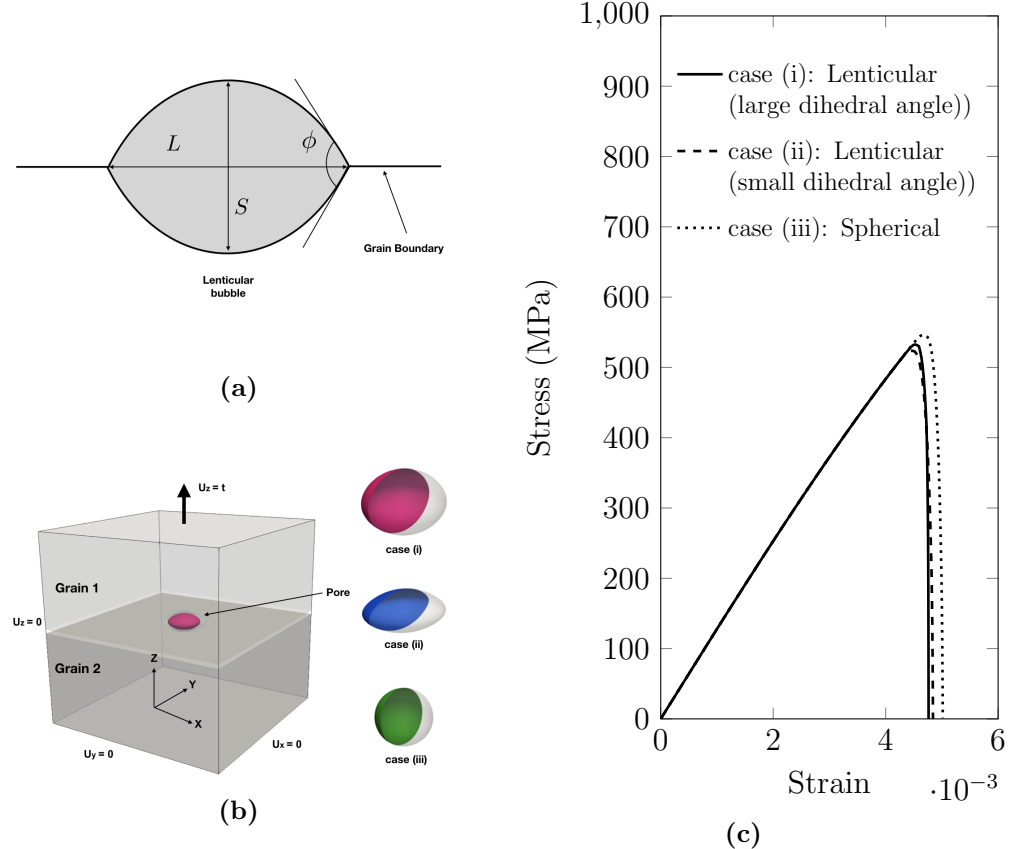


FIGURE 3.7. (a) The lenticular geometry is described by the length  $L$ , the thickness  $S$  and the dihedral angle  $\phi$ . (b) Gas bubble geometry and boundary conditions. (c) Comparison of stress-strain curves for different gas bubble geometries.

### *Effect of loading*

Next, we study the effect of different loading conditions. Uniaxial, biaxial and triaxial loading conditions are considered. The final crack configurations are shown in Figure 3.8. A change in crack path due to a different loading condition is evident from the figure. For uniaxial loading, cracks propagate along the grain boundaries

that are mainly perpendicular to the loading direction. For biaxial loading, crack branching occurs because biaxial loading results in two positive principal components of the strain tensor of the same order of magnitude. For triaxial loading, cracks propagate along all three directions.

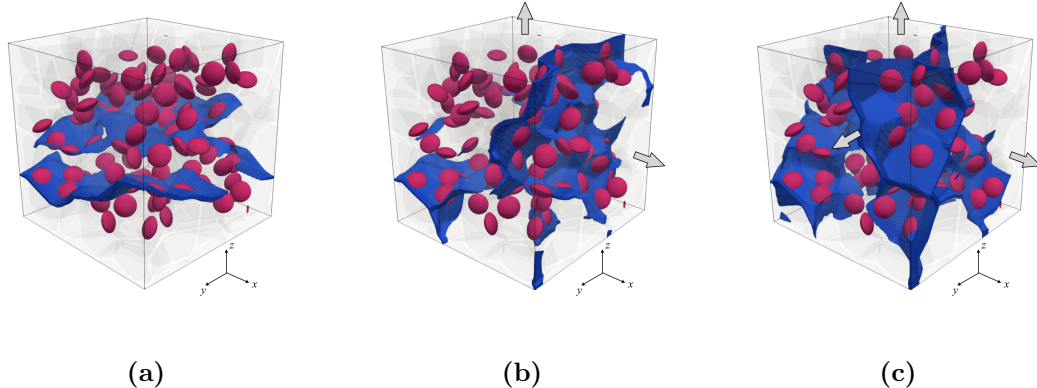


FIGURE 3.8. Final configuration (crack surfaces highlighted in blue) for different loading (a) uniaxial (b) biaxial (c) triaxial.

The stress-strain curves are shown in Figure 3.9. The difference in the slopes during loading is due to the Poisson's effect. The sample under the biaxial and triaxial loading conditions manifest a lower critical fracture strength compared to that under the uniaxial loading condition. The critical strain corresponding to the critical fracture strength under triaxial loading is about half of that under uniaxial loading.

#### *Effect of porosity*

In 2D, under plane-strain assumptions, the porosity represented by a planar bubble is computed by extruding it along the out-of-plane direction, which overestimates the actual porosity. In order to obtain a reasonable correlation between the critical fracture strength and the porosity, a 3D model is necessary.

To study the effect of porosity, consider an REV with side length 40  $\mu\text{m}$ . Grain

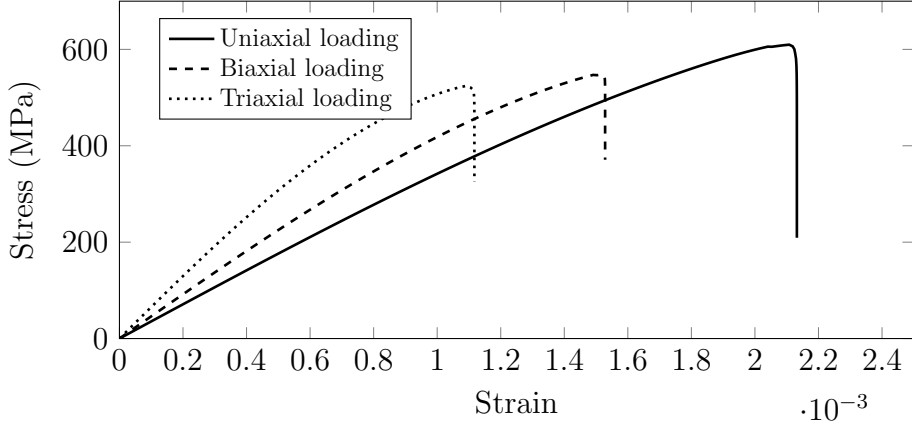


FIGURE 3.9. Comparison of stress-strain curves for different loading conditions.

centroids are generated from a random close-packing (RCP) voronoi structure. The RCP structures can be realized by a spatial sampling process known as Maximal Poisson-disk Sampling (MPS) [24]. For the RCP voronoi structure, the average aspect ratio of each voronoi cell is approximately 1 and an equiaxed grain structure is provided.

The influence of the voronoi structure on fracture properties can be isolated by considering a specific realization of RCP. The realization under consideration consists of 77 grains and the average radius of grains is  $9.4 \mu\text{m}$ . As shown in Figure 3.10, 50, 100 and 150 gas bubbles are randomly distributed over the grain boundaries, with corresponding porosity values 2.02%, 4.04% and 6.06%, respectively. All gas bubbles have a lenticular shape with  $L = 6.4 \mu\text{m}$ ,  $S = 4 \mu\text{m}$ , and  $\phi = 128^\circ$ . Symmetric boundary conditions are prescribed and a uniform displacement is applied on the top of the RVE.

Final configurations of the approximated crack surfaces are shown in Figure 3.10, where, in general, cracks propagate perpendicular to the direction of the applied load.

It is worth noting that cracks keep propagating after initiation without any increase in the applied stress, which suggests that a snap-back is likely to take place

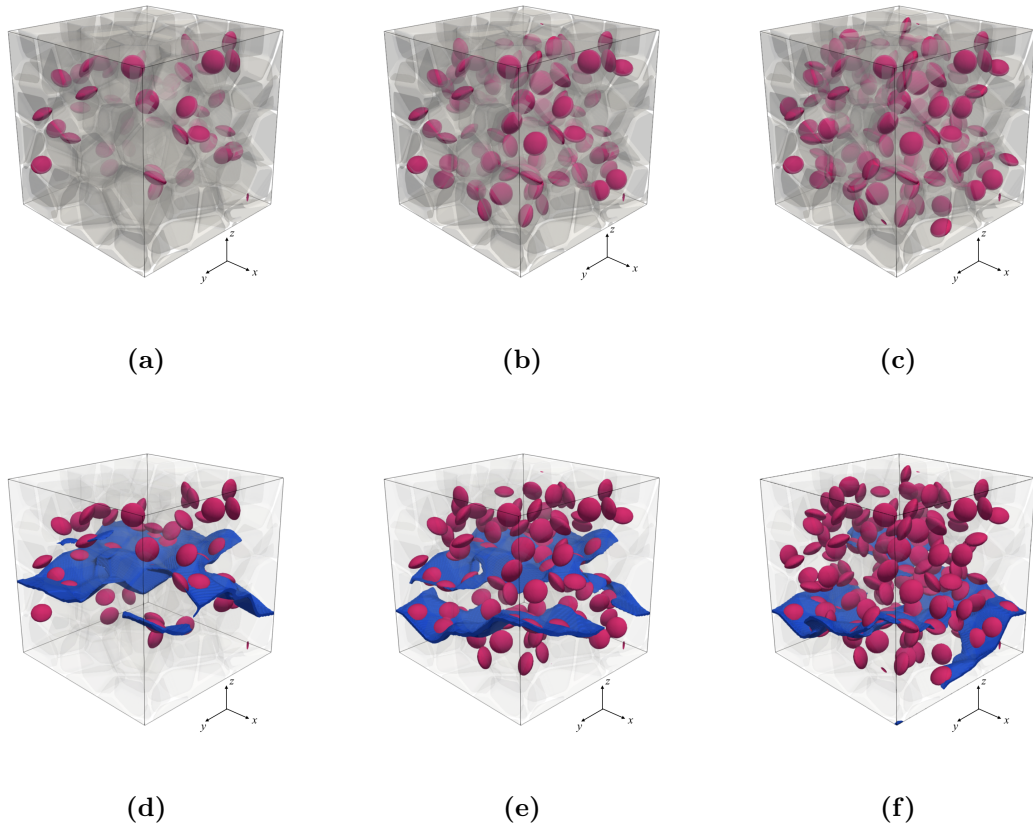


FIGURE 3.10. (a-c) Initial configuration of REVs with an average grain size of  $9.4 \mu\text{m}$ . (d-f) Final configuration (crack surfaces highlighted in blue) for REVs. Different porosity values are considered: (a, d) 2.02%, (b, e) 4.04%, (c, f) 6.06%.

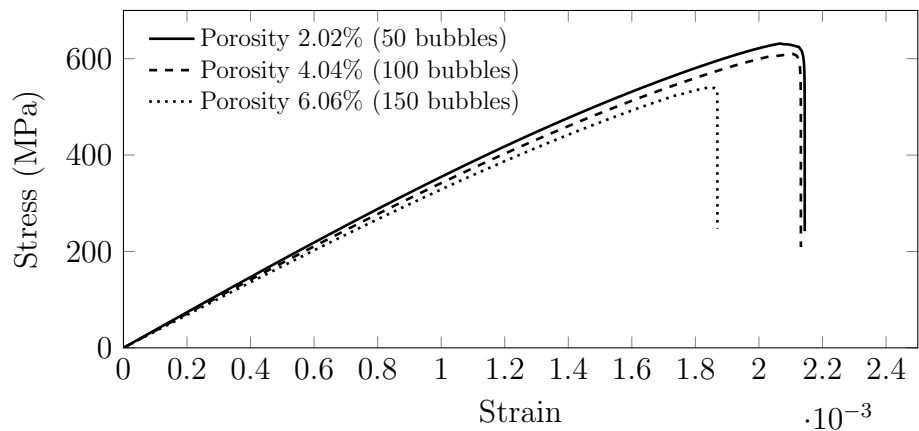


FIGURE 3.11. Comparison of stress-strain curves for different porosity values.

after crack initiation and a mixed force-displacement control is necessary to follow the actual stress-strain curve without loss of information. However, we argue that the a simple displacement control suffices to obtain the critical fracture strength – the maximum stress value along the stress-strain curve. From Figure 3.11, we conclude that an increase in porosity leads to a higher probability of crack initiation at lower stress state and consequently a decrease in the critical fracture strength.

To describe the porosity, average gas bubble and grain size effect on fracture strength, an exponential functional form obtained from biaxial flexure test has been reported in [25]:

$$\frac{\sigma_c}{\sigma_0} = \exp(-a \times \text{porosity}) \quad (3.25)$$

The critical fracture strength is normalized with respect to  $\sigma_0$ . To benchmark with experiments,  $\sigma_0$  is obtained by substituting the average grain and bubble size of 9.4  $\mu\text{m}$  and 5.2  $\mu\text{m}$ . To give proper error bounds on our numerical predictions, five trial calculations were performed on five different realizations of the spatial distribution of bubbles for each porosity level. The fracture strength obtained from 15 realizations of 3 porosity levels is summarized in Table 3.2. The obtained  $\sigma_0$  is 198 MPa, 693 MPa and 697.8 MPa and the coefficient  $a$  is 0.057, 0.14 and 0.04, for experiment, 2D simulations and 3D simulations, respectively. A comparison of the experimental model, previous 2D simulations [12] and current 3D simulations is shown in Figure 3.12. In particular, the 95% confidence interval for the 3D simulations is shown in stripes. It shows that the 3D simulation has significant improvement towards the prediction of the dependence of the critical fracture strength on porosity. It is worth mentioning that the difference between simulation predictions of  $\sigma_0$  and experimental values could be due to the fact that the transgranular fracture observed in experiments [26] has not been incorporated into the current numerical model.

**Table 3.2.** Summary of fracture strength obtained from 15 realizations of 3 porosity values. R denotes the realization index.

Porosity (%)	Critical fracture strength (MPa)				
	R1	R2	R3	R4	R5
2.02	631.4	657.4	645.6	663.4	630.7
4.04	609.8	555.6	605.5	611.2	589.2
6.06	540.0	530.8	557.0	563.2	567.9

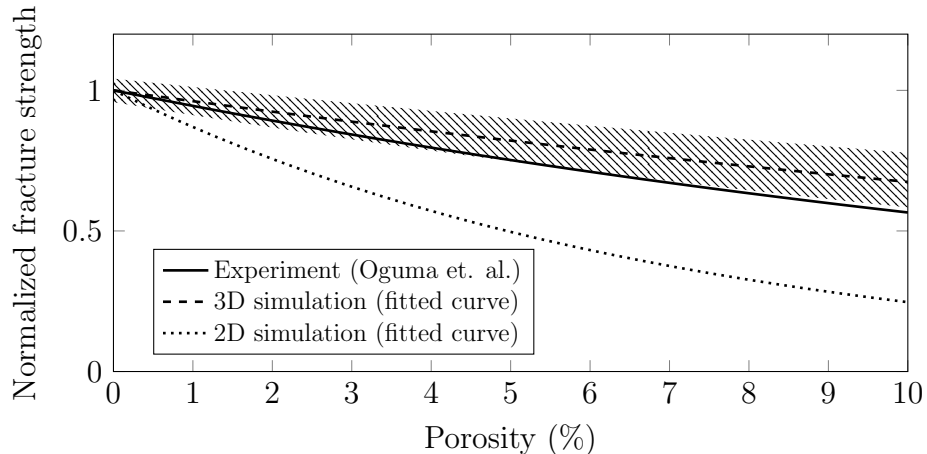


FIGURE 3.12. Variation in normalized fracture strength with changing porosity. In the current chapter, five trial calculations were performed for each porosity level, and each calculation was based on one realization of the spatial distribution of bubbles. The 95% confidence interval is shown in stripes.

### 3.4.2 High burnup structure fragmentation

Next, we adopt the quasi-brittle fracture model to simulate fission-gas-induced intergranular fracture of UO<sub>2</sub> HBS. A two-dimensional REV with side length  $L = 3\text{ }\mu\text{m}$  is considered, and plane-strain conditions are assumed to hold. The material properties and model parameters are summarized in Table 3.3. The critical fracture energy of UO<sub>2</sub> is taken to be 0.022 mJ mm<sup>-3</sup> [27]. Due to the lack of experimental data, the fracture toughness  $\mathcal{G}_c^g$  is assumed to be  $1.2 \times 10^{-6}\text{ mJ mm}^{-3}$  and the Griffith's characteristic length  $l_{ch} = \frac{\mathcal{G}_c}{2\psi_c} \approx 22.78\text{ nm}$ . The domain is uniformly discretized with QUAD4 elements with element size of 0.005 μm.

**Table 3.3.** Parameters and material properties used in the fission-gas-induced HBS fracture simulations.

Property	Symbol	Value	Unit	Reference
Young's modulus	$E$	385	GPa	[20]
Critical fracture energy	$\psi_c$	0.022	$\text{mJ mm}^{-3}$	[27]
Grain boundary fracture toughness	$\mathcal{G}_c^g$	$1.2 \times 10^{-6}$	$\text{mJ mm}^{-3}$	
Grain fracture toughness	$\mathcal{G}_c^b$	$1.2 \times 10^{-5}$	$\text{mJ mm}^{-3}$	
Phase-field regularization length	$l$	0.01	$\mu\text{m}$	

### *LOCA pressure transients*

We begin by investigating gas-pressure-induced fracture during LOCA-driven temperature transients. During a LOCA transient, temperatures in the fuel rod increase rapidly, leading to increased pressure in the gas contained within the bubbles. The temperature as a function of time at the edge of a representative pellet for each rod is obtained from simulation of the Studsvik Rod 196 experiment [28] using the engineering-scale fuel performance code BISON [29]. The temperature transient is used as an input to the Kim-Kim-Suzuki (KKS) phase-field model [30] to determine the pressure as a function of time. In the KKS model, the gas pressure is assumed to be 100 MPa during steady-state reactor operation at 700 K. The Studsvik experiment is initialized with a fixed temperature  $T = 572.6$  K at the outer surface prior to the transient, resulting in a decrease in the pressure from 100 MPa to below 80 MPa. The pressure is assumed to be known in the quasi-brittle fracture model to simulate crack nucleation and propagation in the surrounding regions of the individual bubbles.

Two bubble radii ( $0.25 \mu\text{m}$  and  $0.5 \mu\text{m}$ ) are considered, and no loading is applied on the exterior. The resulting fracture patterns are shown in Figure 3.13. With the smaller bubble, two cracks propagate from the bubble towards the outer surface. With a larger bubble, only one major crack propagates to the free surface, and other minor cracks are arrested. Cracks nucleate when tensile stress on the bubble-matrix

interface reaches the critical fracture strength. The critical pressures are 120.17 MPa and 89.69 MPa for the small and large bubbles, respectively. The critical pressure is significantly lower for the larger bubble.

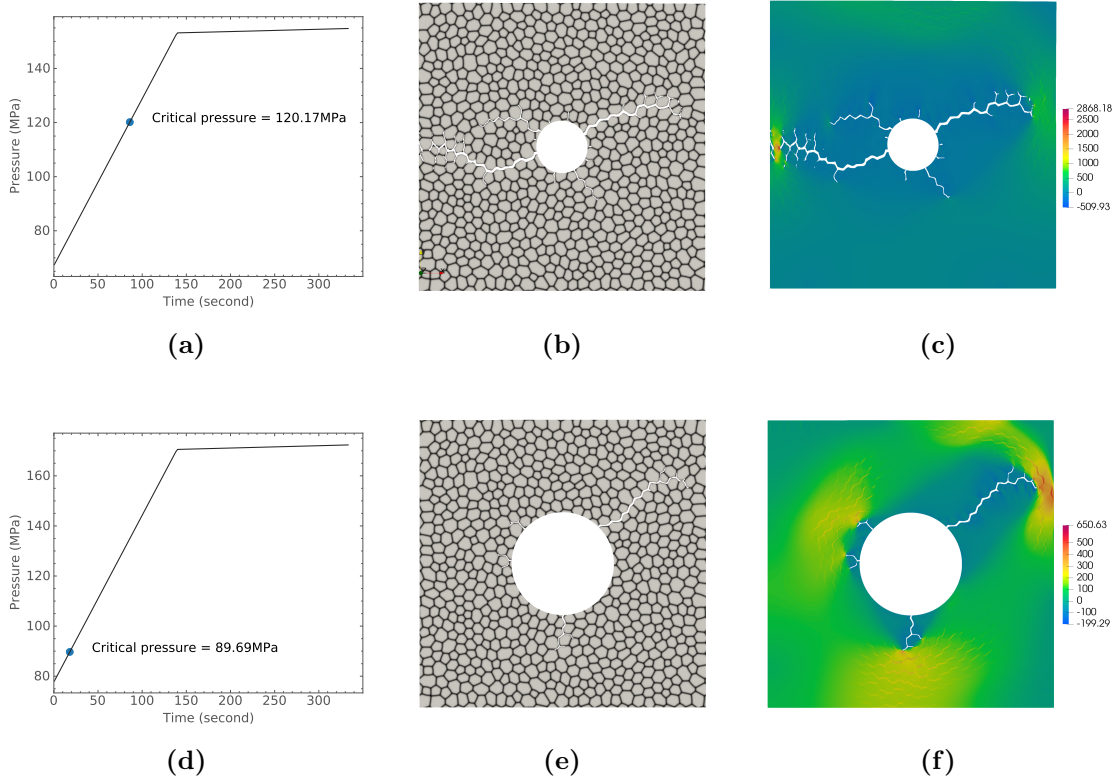


FIGURE 3.13. Results for (a-c) the small bubble with radius 0.25  $\mu\text{m}$  and (d-f) the large bubble with radius 0.25  $\mu\text{m}$  (a, d) Pressure history. (b, e) Crack paths superimposed on the voronoi structure. (c, f) Contour plot of the maximum principal stress.

In a fuel pellet system, external pressure can arise from fuel-cladding mechanical interaction. To study the effect of external pressure, different external pressures are applied on the top and right boundaries. The results from using three different external pressures, 0, 30 MPa, 60 MPa, are shown in Figure 3.14. The critical pressure is significantly higher for larger external pressure values, while there is no qualitative change in the crack pattern.

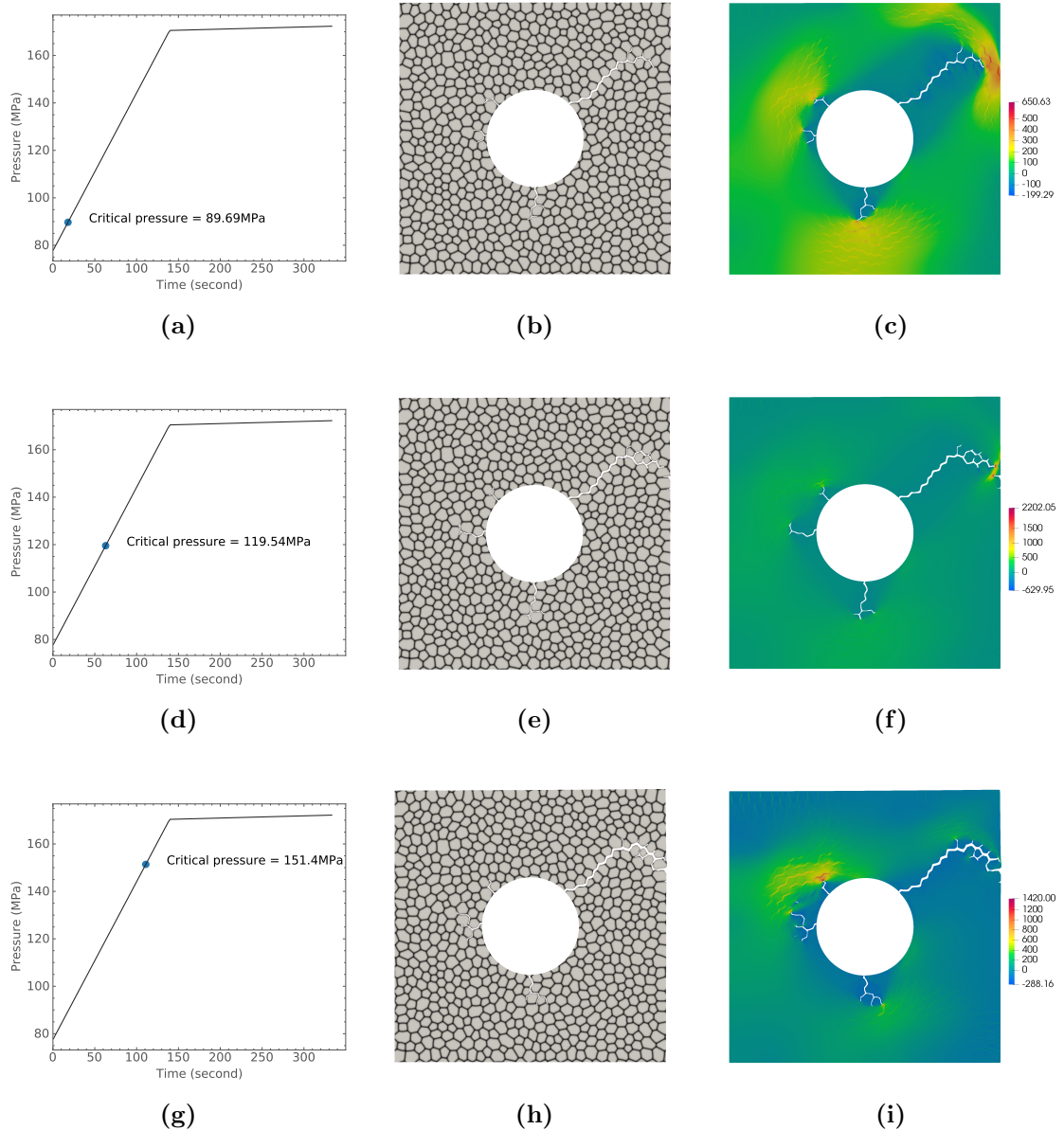


FIGURE 3.14. Results for bubble radius  $0.5 \mu\text{m}$  and external pressure (a-c) 0 MPa, (d-f) 30 MPa, (g-i) 60 MPa. (a, d, g) Pressure history. (b, e, h) Crack paths superimposed on the voronoi structure. (c, f, i) Contour plot of the maximum principal stress.

### *Multi-bubble interaction*

We next investigate the effect of the spatial distribution of the gas bubbles on fragment size. To that end, dimensions are expressed in dimensionless form in this

section. With the origin of the coordinate system placed at the lower left corner of the REV, two cases are considered:

- Two bubbles with centers at  $\left(\frac{2}{15}L, \frac{7}{15}L\right)$  and  $\left(\frac{7}{15}L, \frac{2}{15}L\right)$ .
- Three bubbles with centers at  $\left(\frac{1}{6}L, \frac{8}{15}L\right)$ ,  $\left(\frac{8}{15}L, \frac{1}{6}L\right)$ , and  $\left(\frac{8}{15}L, \frac{8}{15}L\right)$ .

All bubbles have a radius of  $\frac{1}{12}L$ . Results are shown in Figure 3.15. It is observed that the crack paths in cases involving multiple bubbles is strongly affected by the positions of the bubbles relative to each other: Cracks prefer to connect neighboring bubbles. Fully developed cracks and bubbles form a fragment at the lower-left corner in both cases. These fragments consist of multiple grains, and their sizes are affected by the spatial distribution of bubbles.

### *Partial HBS*

Lastly, we use the output from the HBS formation simulations as our initial condition. In this case, the initial condition is generated from the phase field simulations that explicitly model the defect evolution, and recrystallization behavior leading to HBS formation. A detailed description of the model can be found in [30]. Considering that fragmentation has been observed in partially recrystallized zones, we focused on the fracture behavior of the partial HBS obtained from these simulations. Three HBS at different recrystallization stages with 25%, 60%, and 100% recrystallization fraction were considered. A linearly increasing pressure was applied. For all three cases, crack initiation occurred at around 60 MPa, thanks to their similar bubble sizes. Crack initiation locations varied among the three cases, since more grains form around the bubble during recrystallization and their points of intersection with the bubble can become possible initiation sites. In addition, the recrystallized grain

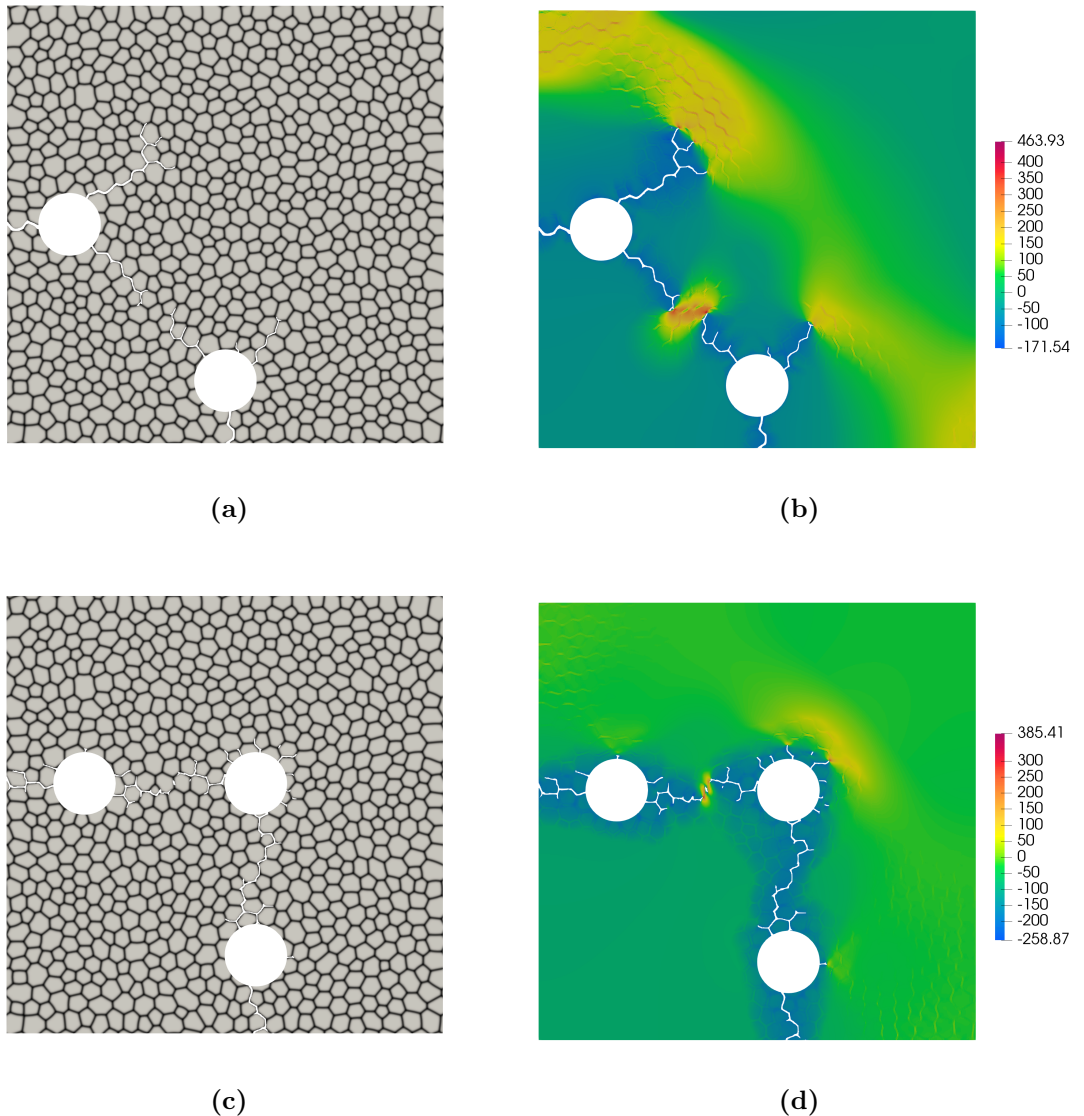


FIGURE 3.15. Results for (a-b) the two-bubble case and (c-d) the three-bubble case. (a, c) Crack paths superimposed on the voronoi structure. (b, d) Contour plot of the maximum principal stress.

structures change the grain boundary morphology, thus altering crack propagation directions and paths.

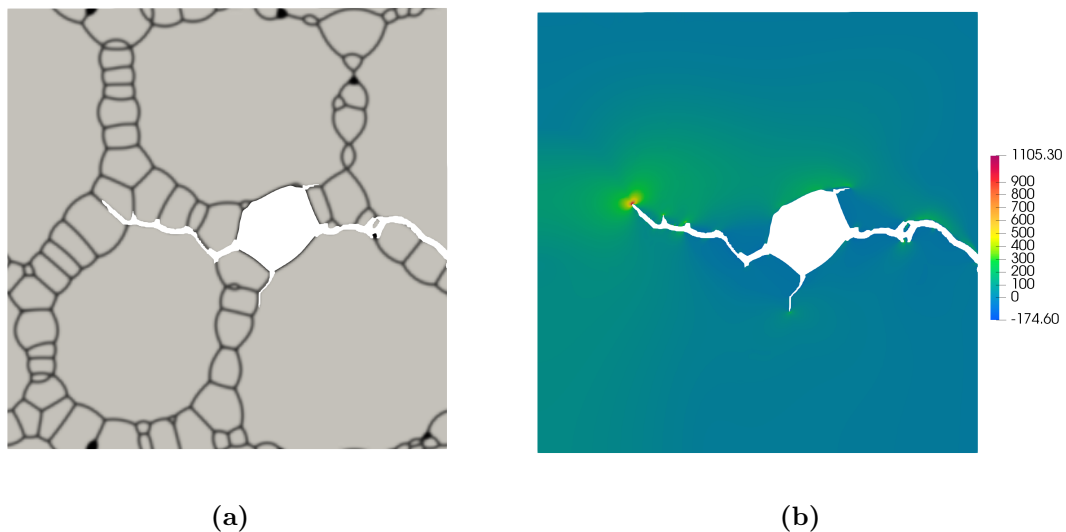


FIGURE 3.16. 25 % recrystallization stage: (a) Crack propagation; (b) Maximum principal stress.

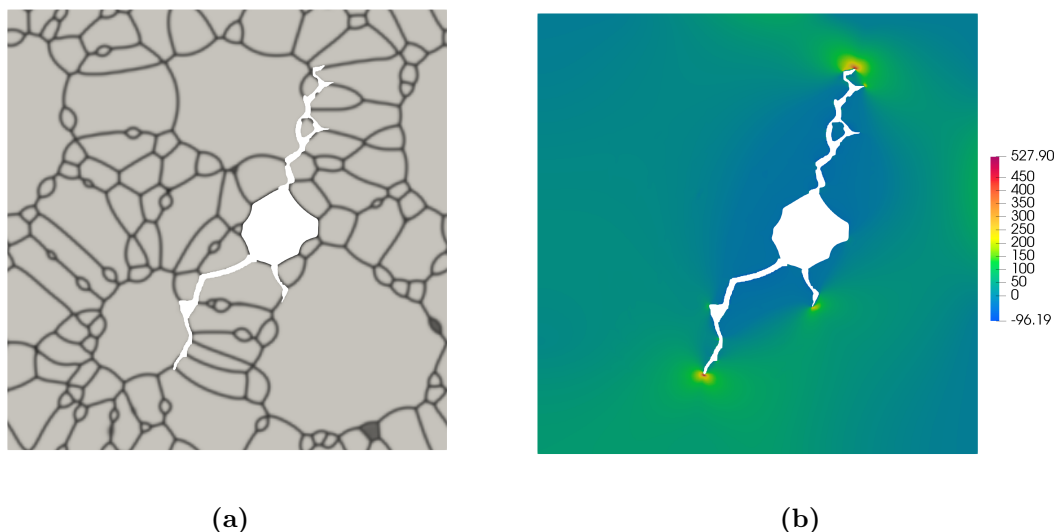


FIGURE 3.17. 60 % recrystallization stage: (a) Crack propagation; (b) Maximum principal stress.

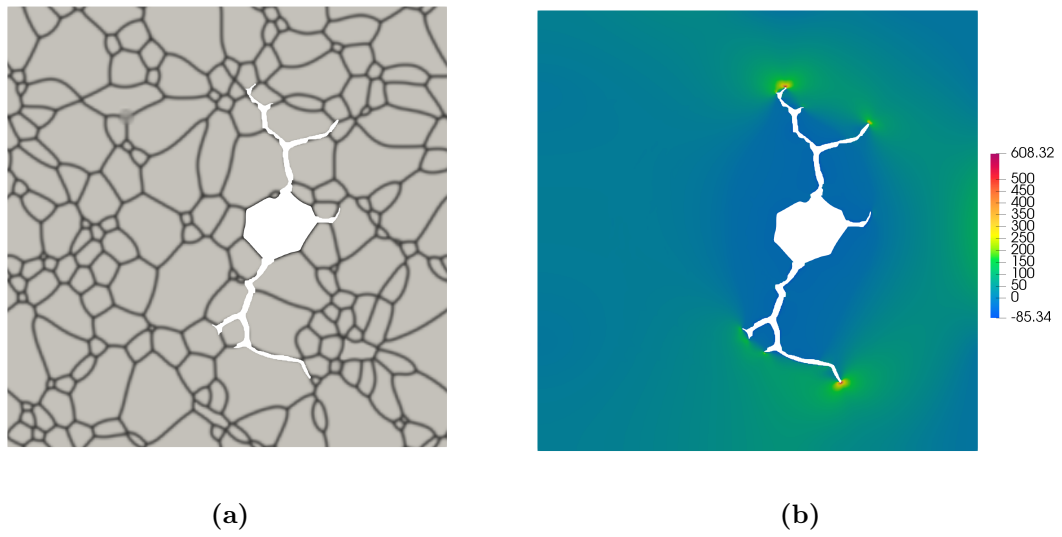


FIGURE 3.18. 100 % recrystallization stage: (a) Crack propagation; (b) Maximum principal stress.

# **Appendix A**

Code availability

## **Appendix B**

On the phase-field irreversibility constraint

# Appendix C

## The flooding algorithm for counting fragments

We describe the algorithm for clustering various elements in a mesh to individual fragments, as delineated by a damage field. The algorithm assigns each element a cluster order parameter, and different clusters are separated by a band of “broken” elements where the damage is above a threshold, i.e.  $d > d_{\text{th}}$ . Figure C.1 provides an example of this algorithm for a representative damage field.

The algorithm has a fundamental “flooding” structure. In particular, a seeding element broadcasts its information to all of its geometric neighbors, and each neighbor becomes a new seed for the next round of information propagation. In the context of counting fragments, the information of an element includes its state and the cluster it belongs to. An element is considered to be “intact” if all of its nodal damage values are below  $d_{\text{th}}$ , otherwise it is considered to be “broken”.

Three lists are managed by the algorithm. The first list **ALL** includes all elements that need to be classified. The second list **CANDIDATE**, optionally a first-in-first-out (FIFO) queue, includes all candidate elements for the current cluster. The third list **BROKEN** includes all “broken” elements. Each cluster  $\text{CLUSTER}^i$  is essentially a list of

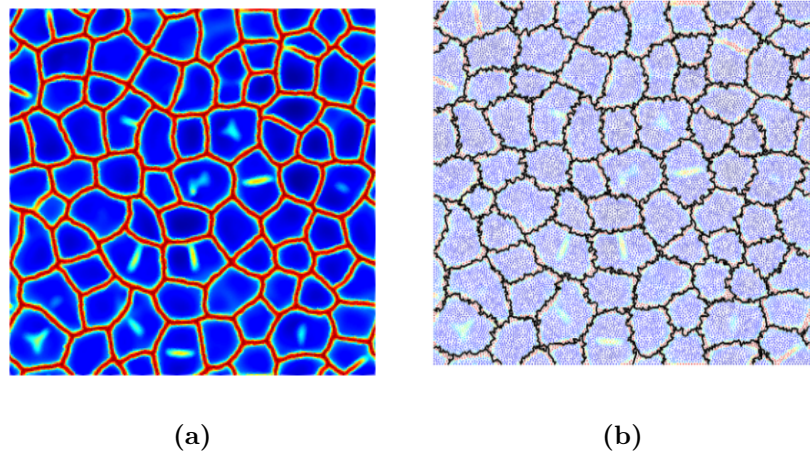


FIGURE C.1. (a) Final damage field obtained using a spatially correlated random  $\mathcal{G}_c$  and  $\psi_c$ . (b) Corresponding clusters labeled by the flooding algorithm. Cluster boundaries are marked in black.

elements that belong to the same parent cluster.

The algorithm consists of three stages. In the first stage, we update the damage values of all nodes and states of all elements. All elements that have a status change require reclassification. Therefore, any cluster that contains elements pending reclassification is pushed into **ALL** for future reclassification.

In the second stage, all “intact” elements in **ALL** are pushed into **CANDIDATE** one at a time until **ALL** has no more “intact” elements. Each new cluster is constructed by dequeuing **CANDIDATE**. The first element in **CANDIDATE** is dequeued after all of its connecting “intact” elements from **ALL** are pushed into **CANDIDATE**.

During the third stage, “broken” elements are grouped into their nearest cluster to preserve the total volume of the mesh. In our implementation, “broken” elements are assigned to clusters based on the solution to a minimization problem of weighted Euclidean distance between the elements and cluster centroids.

The skeleton of the flooding algorithm is outlined in Algorithm 1.

---

**Algorithm 1** An iterative flooding algorithm for fragmentation count

---

```
1: Set  $d_0 \leftarrow 0$ 
2: Set cluster count  $c \leftarrow 0$ 
3: Group all elements into  $\text{CLUSTER}^c$ 
4: for time step  $n \in \{0, 1, 2, \dots\}$  do
5:   for each cluster  $\text{CLUSTER}^i$  do
6:     Move all “broken” elements into  $\text{BROKEN}$ 
7:     if  $\text{CLUSTER}^i$  contains any element that has a state change, i.e. from “intact” to “broken” then
8:       Move all remaining elements into  $\text{ALL}$ 
9:     end if
10:    end for
11:    while  $\text{ALL}$  is not empty do
12:      if All elements in  $\text{ALL}$  are “broken” then
13:        Move all elements in  $\text{ALL}$  into  $\text{BROKEN}$ 
14:        Break while loop
15:      else
16:        Move one “intact” element from  $\text{ALL}$  to  $\text{CANDIDATE}$ 
17:        Increment cluster count  $c \leftarrow c + 1$ 
18:        while  $\text{ALL}$  is not empty do
19:          for each element  $e$  that shares a common edge with the first element
in the queue  $\text{CANDIDATE}$  do
20:            if  $e$  is “intact” then
21:              Enqueue  $e$  into  $\text{CANDIDATE}$ 
22:            else
23:              Move  $e$  into  $\text{BROKEN}$ 
24:            end if
25:          end for
26:          Dequeue first element in  $\text{CANDIDATE}$  into  $\text{CLUSTER}^c$ 
27:        end while
28:      end if
29:    end while
30:    Move all elements in  $\text{BROKEN}$  into their nearest cluster
31: end for
```

---

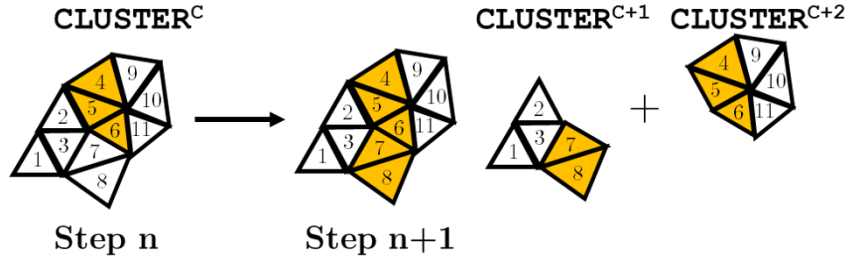


FIGURE C.2. Status change from step  $n$  to step  $n+1$ . “Broken” elements are labeled in yellow, and “intact” elements are white. The step-by-step reclassification procedure is shown in Table C.1.

**Table C.1.** Demonstration of classification after the update from time step  $n$  to time step  $n+1$ . Broken elements are denoted with an underscore.

Step	Stage	ALL	CANDIDATE	BROKEN	Comments
$n$		$\emptyset$	$\emptyset$	$\emptyset$	$CLUSTER^c = \{1, 2, 3, \underline{4}, \underline{5}, \underline{6}, 7, 8, 9, 10, 11\}$
$n+1$		$\emptyset$	$\emptyset$	$\emptyset$	$CLUSTER^c = \{1, 2, 3, \underline{4}, \underline{5}, \underline{6}, \underline{7}, \underline{8}, 9, 10, 11\}$
$n+1$	1	$\{1, 2, 3, 9, 10, 11\}$	$\emptyset$	$\{\underline{4}, \underline{5}, \underline{6}, 7, 8\}$	Declassify $CLUSTER^c$
$n+1$	2	$\{2, 3, 9, 10, 11\}$	$\{1\}$	$\{\underline{4}, \underline{5}, \underline{6}, 7, 8\}$	Enqueue element 1 to CANDIDATE
$n+1$	2	$\{9, 10, 11\}$	$\{1, 2, 3\}$	$\{\underline{4}, \underline{5}, \underline{6}, 7, 8\}$	Enqueue connected elements 2, 3
$n+1$	2	$\{9, 10, 11\}$	$\{2, 3\}$	$\{\underline{4}, \underline{5}, \underline{6}, 7, 8\}$	Dequeue element 1
$n+1$	2	$\{9, 10, 11\}$	$\{3\}$	$\{\underline{4}, \underline{5}, \underline{6}, 7, 8\}$	Dequeue element 2
$n+1$	2	$\{9, 10, 11\}$	$\emptyset$	$\{\underline{4}, \underline{5}, \underline{6}, 7, 8\}$	Dequeue element 3
$n+1$	2	$\{10, 11\}$	$\{9\}$	$\{\underline{4}, \underline{5}, \underline{6}, 7, 8\}$	$CLUSTER^{c+1} = \{1, 2, 3\}$
$n+1$	2	$\emptyset$	$\{9, 10, 11\}$	$\{\underline{4}, \underline{5}, \underline{6}, 7, 8\}$	Enqueue element 9 to CANDIDATE
$n+1$	2	$\emptyset$	$\{10, 11\}$	$\{\underline{4}, \underline{5}, \underline{6}, 7, 8\}$	Enqueue connected elements 10, 11
$n+1$	2	$\emptyset$	$\{11\}$	$\{\underline{4}, \underline{5}, \underline{6}, 7, 8\}$	Dequeue element 9
$n+1$	2	$\emptyset$	$\emptyset$	$\{\underline{4}, \underline{5}, \underline{6}, 7, 8\}$	Dequeue element 10
$n+1$	2	$\emptyset$	$\emptyset$	$\{\underline{4}, \underline{5}, \underline{6}, 7, 8\}$	Dequeue element 11
$n+1$	3	$\emptyset$	$\emptyset$	$\{\underline{4}, \underline{5}, \underline{6}\}$	Group elements 7, 8 into $CLUSTER^{c+1}$
$n+1$	3	$\emptyset$	$\emptyset$	$\emptyset$	Group elements 4, 5, 6 into $CLUSTER^{c+2}$

# Bibliography

- [1] Gianni Dal Maso. *An introduction to  $\Gamma$ -convergence*, volume 8. Springer Science & Business Media, 2012.
- [2] Qiang Yang, Laurent Stainier, and Michael Ortiz. A variational formulation of the coupled thermo-mechanical boundary-value problem for general dissipative solids. *Journal of the Mechanics and Physics of Solids*, 54(2):401–424, 2006.
- [3] Timo Heister, Mary F Wheeler, and Thomas Wick. A primal-dual active set method and predictor-corrector mesh adaptivity for computing fracture propagation using a phase-field approach. *Computer Methods in Applied Mechanics and Engineering*, 290:466–495, 2015.
- [4] Satish Balay, Shrirang Abhyankar, Mark F. Adams, Jed Brown, Peter Brune, Kris Buschelman, Lisandro Dalcin, Alp Dener, Victor Eijkhout, William D. Gropp, Dmitry Karpeyev, Dinesh Kaushik, Matthew G. Knepley, Dave A. May, Lois Curfman McInnes, Richard Tran Mills, Todd Munson, Karl Rupp, Patrick Sanan, Barry F. Smith, Stefano Zampini, Hong Zhang, and Hong Zhang. PETSc Web page. <https://www.mcs.anl.gov/petsc>, 2019. URL <https://www.mcs.anl.gov/petsc>.
- [5] Tianchen Hu, Johann Guilleminot, and John E Dolbow. A phase-field model of fracture with frictionless contact and random fracture properties: Application to thin-film fracture and soil dessication. *Computer Methods in Applied Mechanics and Engineering*, 368:113106, 2020.
- [6] Nathan Capps, Colby Jensen, Fabiola Cappia, Jason Harp, Kurt Terrani, Nicolas Woolstenhulme, and Daniel Wachs. A critical review of high burnup fuel fragmentation, relocation, and dispersal under loss-of-coolant accident conditions. *Journal of Nuclear Materials*, 546:152750, 2021.
- [7] Vincenzo V. Rondinella and Thierry Wiss. The high burn-up structure in nuclear fuel. *Materials Today*, 13(12):24–32, 2010.
- [8] J. A. Turnbull, S. K. Yagnik, M. Hirai, D. M. Staicu, and C. T. Walker. An assessment of the fuel pulverization threshold during loca-type temperature transients. *Nuclear Science and Engineering*, 179(4):477–485, 2015.

- [9] Wen Jiang, Benjamin W. Spencer, and John E. Dolbow. Ceramic nuclear fuel fracture modeling with the extended finite element method. *Engineering Fracture Mechanics*, 223:106713, 2020. ISSN 0013-7944.
- [10] Katalin Kulacsy. Mechanistic model for the fragmentation of the high-burnup structure during loca. *Journal of Nuclear Materials*, 466:409 – 416, 2015.
- [11] Lars O. Jernkvist. A review of analytical criteria for fission gas induced fragmentation of oxide fuel in accident conditions. *Progress in Nuclear Energy*, 119:103188, 2020. ISSN 0149-1970.
- [12] Pritam Chakraborty, Yongfeng Zhang, and Michael R. Tonks. Multi-scale modeling of microstructure dependent intergranular brittle fracture using a quantitative phase-field based method. *Computational Materials Science*, 113:38 – 52, 2016. ISSN 0927-0256.
- [13] Martin Diehl, Marcel Wicke, Pratheek Shanthraj, Franz Roters, Angelika Brueckner-Foit, and Dierk Raabe. Coupled crystal plasticity–phase field fracture simulation study on damage evolution around a void: Pore shape versus crystallographic orientation. *JOM*, 69(5):872–878, May 2017.
- [14] Chukwudi Chukwudzie, Blaise Bourdin, and Keita Yoshioka. A variational phase-field model for hydraulic fracturing in porous media. *Computer Methods in Applied Mechanics and Engineering*, 347:957 – 982, 2019.
- [15] Andro Mikelić, Mary F Wheeler, and Thomas Wick. A quasi-static phase-field approach to pressurized fractures. *Nonlinearity*, 28(5):1371–1399, apr 2015.
- [16] Jian-Ying Wu. A unified phase-field theory for the mechanics of damage and quasi-brittle failure. *Journal of the Mechanics and Physics of Solids*, 103:72 – 99, 2017.
- [17] Zachary A. Wilson and Chad M. Landis. Phase-field modeling of hydraulic fracture. *Journal of the Mechanics and Physics of Solids*, 96:264 – 290, 2016. ISSN 0022-5096.
- [18] Keita Yoshioka, Dmitri Naumov, and Olaf Kolditz. On crack opening computation in variational phase-field models for fracture. *Computer Methods in Applied Mechanics and Engineering*, 369:113210, 2020.
- [19] B. Bourdin, G.A. Francfort, and JJ Marigo. The variational approach to fracture. *Journal of Elasticity*, 91:5 – 148, 2008.
- [20] K. Govers. Comparison of interatomic potentials for UO<sub>2</sub>. *Journal of Nuclear Materials*, 366:161–177, 2007.

- [21] N. Moelans, B. Blanpain, and P. Wollants. Quantitative analysis of grain boundary properties in a generalized phase field model for grain growth in anisotropic systems. *Phys. Rev. B*, 78:024113, Jul 2008.
- [22] E.N. Hodkin. The ratio of grain boundary energy to surface energy of nuclear ceramics as determined from pore geometries. *Journal of Nuclear Materials*, 88(1):7 – 14, 1980. ISSN 0022-3115.
- [23] G.L. Reynolds, W.B. Beeré, and P.T. Sawbridge. The effect of fission products on the ratio of grain-boundary energy to surface energy in irradiated uranium dioxide. *Journal of Nuclear Materials*, 41(1):112 – 114, 1971. ISSN 0022-3115.
- [24] Mohamed S. Ebeida, Scott A. Mitchell, Anjul Patney, Andrew A. Davidson, and John D. Owens. A simple algorithm for maximal poisson-disk sampling in high dimensions. *Computer Graphics Forum*, 31(2pt4):785–794, 2012.
- [25] M. Oguma. Microstructure effects on fracture strength of UO<sub>2</sub> fuel pellets. *Journal of Nuclear Science and Technology*, 19(12):1005–1014, 1982.
- [26] A. G. Evans and R. W. Davidge. The strength and fracture of stoichiometric polycrystalline UO<sub>2</sub>. *Journal of Nuclear Materials*, 33:249–260, 1969.
- [27] M. Oguma. Microstructure effects on fracture strength of u02 fuel pellets. *Journal of Nuclear Science and Technology*, 19(12):1005–1014, 1982.
- [28] Anders Puranen. Post test examinations on loca tested rods. Studsvik Report STUDSVIK/N-13/198, Studsvik, 2013.
- [29] R. L. Williamson, J. D. Hales, S. R. Novascone, G. Pastore, K. A. Gamble, B. W. Spencer, W. Jiang, S. A. Pitts, A. Casagrande, D. Schwen, A. X. Zabriskie, A. Toptan, R. Gardner, C. Matthews, W. Liu, , and H. Chen. Bison: A flexible code for advanced simulation of the performance of multiple nuclear fuel forms. *Nuclear Technology*, 2020.
- [30] L. K. Aagesen, S. Biswas, W. Jiang, A. M. Jokisaari, D. Andersson, M. W. D. Cooper, and C. Matthews. Determine fragmentation criteria in high-burnup uo<sub>2</sub> fuel during accident conditions. Technical Report INL/EXT-20-00558, Idaho National Laboratory, 2020.

# **Biography**

About myself.